Journal of Computational Physics 473 (2023) 111755

Contents lists available at ScienceDirect

Journal of Computational Physics

journal homepage: www.elsevier.com/locate/jcp

Hybrid discontinuous Galerkin-finite volume techniques for compressible flows on unstructured meshes

Vadim Maltsev, Dean Yuan, Karl W. Jenkins, Martin Skote, Panagiotis Tsoutsanis *

Centre for Computational Engineering Sciences, Cranfield University, Cranfield MK43 0AL, United Kingdom

ARTICLE INFO

Article history:
Received 27 July 2022
Received in revised form 31 October 2022
Accepted 3 November 2022
Available online xxxx

Keywords:
Hybrid DG-FV
Unstructured meshes
Troubled cell indicators
Supersonic civil airliner
UCNS3D

ABSTRACT

In this paper we develop a family of arbitrarily high-order non-oscillatory hybrid Discontinuous Galerkin(DG)-Finite Volume(FV) schemes for mixed-element unstructured meshes. Their key ingredient is a switch between a DG method and a FV method based on the CWENOZ scheme when invalid solutions are detected by a troubled cell indicator checking the unlimited DG solution. Therefore, the high order of accuracy offered by DG is preserved in smooth regions of the computational domain, while the robustness of FV is utilized in regions with strong gradients. The high-order CWENOZ variant used has the same spatial order of accuracy as the DG variant, while representing one of the most compact applications on unstructured meshes, therefore simplifying the implementation, reducing the computational overhead associated with large stencils of the original WENO reconstruction without sacrificing the desirable non-oscillatory properties of the schemes. We carefully investigate several parameters associated with the switching between DG and FV methods including the troubled cell indicators in *a priori* fashion. For the first time in the literature, we investigate the definition of the bounds for an admissible solution, the frequency by which we use the troubled cell indicators, and the evolution of the percentage of troubled cells for unsteady test problems. The 2D and 3D Euler equations are solved for well established test problems and compared with computational or experimental reference solutions. All the methods have been implemented and deployed within the `UCNS3D` open-source high-order unstructured Computational Fluid Dynamics (CFD) solver. The present coupling has the potential to improve the shortcomings of both FV-DG in a computational efficient manner. The improved accuracy and robustness provided is a characteristic of paramount importance for industrial-scale CFD applications, and favours the extension to other systems of governing equations.

1. Introduction

Originally introduced for the solution of the linear neutron transport equation by Reed and Hill [1], the Discontinuous Galerkin method was later extended to the solution of general non-linear hyperbolic conservation laws by a series of papers by Cockburn and Shu [2–4], and it is nowadays a popular and advantageous choice in the context of high-order, parallel

* Corresponding author.
E-mail addresses: v.maltsev@cranfield.ac.uk (V. Maltsev), dean.yuan@cranfield.ac.uk (D. Yuan), k.w.jenkins@cranfield.ac.uk (K.W. Jenkins), m.skote@cranfield.ac.uk (M. Skote), panagiotis.tsoutsanis@cranfield.ac.uk (P. Tsoutsanis).

https://doi.org/10.1016/j.jcp.2022.111755

and unstructured CFD codes. The main idea of the DG method is to represent the solution through a piecewise polynomial expansion over a set of basis functions, avoiding any reconstruction on large stencils. Instead, the time evolution of each degree of freedom in each cell involves only the direct neighbouring elements.

The DG method is able to share many features typical of the FV framework, such as the explicit high-order Runge-Kutta time stepping discretisation (RKDG) and the application of exact or approximate Riemann solvers at cell interfaces. Furthermore, assuming the numerical flux to be continuous and monotone, the DG method is stable in L_2 norm as the local cell entropy inequality is satisfied [5].

However, the DG method still suffers from the classical drawback of high-order accuracy methods in terms of the Godunov order-barrier theorem, i.e. it is prone to exhibit oscillations in presence of discontinuities, known as the Gibbs phenomenon, which can lead to unbounded and unphysical solutions. Again, a number of techniques developed originally for the FV method were successfully adapted to the DG method, see for instance the slope limiter of the *minmod* type [6], carrying total variation bounded (TVB) properties, or the moment based limiters [7,8]. The great disadvantage of such limiters is the potential accuracy degradation of the solution in smooth flow regions, where the limiter is mistakenly activated. For this reason, in the FV context, the standard choice to avoid accuracy degradation is to use essentially non-oscillatory (ENO) or weighted ENO (WENO) schemes [9–13], able to achieve in most cases both high-order accuracy and non-oscillatory properties thanks to a non-linear reconstruction procedure operating on large stencils.

Classical WENO schemes aim to reproduce a high-order interpolating polynomial by means of a convex combination of lower-order polynomials having directional stencils, whose width on unstructured meshes depends on the quality of the elements, reflecting on the difficulty of choosing an optimal value for the linear weights used for the convex combination, as well as increasing the complexity in communications across different CPUs in parallel codes. In addition, it is not guaranteed that the reconstruction is able to retrieve non-oscillatory information, as it may happen that none of the stencils lay in a adequately smooth flow region.

In order to alleviate these shortcomings, the Compact WENO (CWENO) schemes, introduced by Levy et al. [14] for a 3^{rd} order reconstruction in the one-dimensional case, and later extended to arbitrarily high-order accuracy and non-uniform meshes [15,16], propose to reduce the order of the directional stencils, enhancing efficiency and robustness of the scheme. Here the directional stencils are contained in the central stencil, and in smooth regions the central stencil order is recovered, whereas in discontinuous regions the chances to have at least one directional stencil with smooth data variation are increased. The accuracy of the scheme can be further enhanced by a linear combination of lower order smoothness indicators like in WENOZ schemes [17,18]. Thanks to their compact size, the CWENO/CWENOZ schemes are more suitable to be used in conjunction with the DG framework. However, in order to preserve the accuracy and compactness properties of the original DG method, the limiting procedure should still be applied only where necessary.

For this reason, the limiting strategy usually consists of two steps [19–22]. First, the so-called *troubled cells* where the limiting procedure need to be applied are determined through a troubled cell detector. Then, the higher modes of the unlimited DG solution are replaced with the WENO reconstructed degrees of freedom (DOFs), where the cell average of the new polynomial must coincide with that of the DG polynomial in order to ensure conservation.

Assuming that the non-linear reconstruction is able to maintain the original order of convergence, the first step is of great importance in the sense that the troubled cell detector needs to be sensitive enough to capture all the oscillations while only being activated in discontinuous flow regions. A multitude of indicators were proposed in the literature in recent years, starting from the TVB derived detector proposed in [3] to the detectors based on the superconvergence properties of the DG method like the ones developed in [23,24]. The whole procedure presented above falls into the *a priori* type of limiting procedure, i.e. the solution checking and the reconstruction happens before the flux reconstruction, thus operating always on the same time level. Alternatively, the solution checking can be performed after the time advancement, in *a posteriori* fashion [25,26], enabling the choice of simpler checking criteria and also enhancing the robustness of the whole procedure. The downside is an increase in computational cost, as when the solution in a cell is discarded, the neighbouring elements also need to be recomputed to “repair” any contamination occurred during the fluxes computation.

The solution checking criteria used in such methods, usually referred to as Multi-Dimensional Optimal Order Detection (MOOD) and specifically the Physical Admissible Detector (PAD) and Numerical Admissible Detector (NAD) [13,27–29], are also attractive indicators in the context of the *a priori* limiting procedure for hybrid DG-FV schemes. However, it is not fully clear from literature if a cell is allowed to be valid at further time stages after it is deemed as troubled at the beginning of the time stepping procedure, and how this affects the evolution of the troubled cell population.

In addition, the majority of the above troubled cell indicators use threshold value(s) that often need to be adjusted based on the order of the scheme, mesh resolution, and the typology of the test problem itself. The selection of the threshold value is driven by the degree of oscillations allowed in the solution without sacrificing accuracy, although that is not the only factor to play a key part in such hybridisation of the DG scheme with FV type reconstruction.

An important aspect in the FV reconstruction that transfers to the quality of the DG-FV hybridisation is the bounds within which the validity of the solution is checked. The first step in the reconstruction procedure consists of the stencil assembly. The number of layers determining the size of the stencil, which in turn depends on arguments like compactness and mesh elements quality, not only influences the performance of the reconstruction but also the number of troubled cells that the detector marks. This aspect was investigated within the MUSCL framework in [30], where it was demonstrated that the limiter can be mistakenly activated, leading to sub-optimal order of accuracy, if the bounds are established only

within the direct side neighbours. In this paper, we investigate with similar considerations the impact of different bounds definitions on the threshold limit of troubled cell detectors, and the situations in which this can be relaxed.

All the schemes are developed in the open source UCNS3D solver [31,32], and we assess their performance in terms of robustness, accuracy and computational efficiency for a series of stringent 2D and 3D test problems. The paper is organized as follows: in Section 2 we introduce the numerical framework used to describe the high-order Discontinuous Galerkin and Finite Volume frameworks for unstructured meshes, the reconstruction process for the CWENOZ scheme, and the numerical fluxes and temporal discretisation employed. The numerical results obtained for all the test problems are presented in Section 3 and compared against analytical, reference or experimental solutions whenever those are available. Section 4 describes the conclusions drawn from this study.

2. Numerical framework

2.1. Discontinuous Galerkin method

In DG methods, higher orders of accuracy are attained by means of a high-order polynomial representation of the local element solution. Similar to FV schemes, as the solution is discontinuous across the domain elements, the treatment of the flux may be dealt with numerically by introducing a Riemann solver.

Consider the unsteady non-linear hyperbolic system of conservation laws on a 3D domain Ω, written in its conservative form:

$$\frac{\partial \mathbf{U}}{\partial t} + \nabla \cdot (\mathbf{F}(\mathbf{U})) = 0, \tag{1}$$

where $\mathbf{U} = \mathbf{U}(\mathbf{x}, t)$ is the vector of conserved variables, $\mathbf{x} = (x, y, z)$ denotes the coordinates of a point of the domain Ω, and $\mathbf{F}(\mathbf{U}) = (\mathbf{f}(\mathbf{U}), \mathbf{g}(\mathbf{U}), \mathbf{h}(\mathbf{U}))$ is the non-linear flux tensor. The physical domain Ω consists of any combination of conforming tetrahedral, hexahedral, prism or pyramids in 3D, and quadrilateral or triangular in 2D. All the elements are indexed by a unique mono-index i. The global solution is discretely approximated for each cell i by a set of locally continuous piecewise solutions $\mathbf{U}_i(\mathbf{x})$. The local approximation of the solution within each cell i, is given by a linear combination of a basis functions $\phi_i^k(\mathbf{x})$ as follows:

$$\mathbf{U}_i(\mathbf{x}) = \sum_{k=0}^{K} \mathbf{U}_{h,i}^k \phi_i^k(\mathbf{x}). \tag{2}$$

We take the weak form of the DG formulation, which is obtained multiplying Eq. (1) by a smooth test function $\psi(\mathbf{x})$, integrating over each element $V_i \in \Omega$ and performing an integration by parts:

$$\int_{V_i} \psi(\mathbf{x}) \frac{\partial \mathbf{U_i}}{\partial t} dV = \int_{V_i} \nabla \psi(\mathbf{x}) \cdot \mathbf{F}(\mathbf{U}_i) dV - \oint_{S_i} \psi(\mathbf{x}) \mathbf{F}(\mathbf{U}_i) \cdot \mathbf{n} dS. \tag{3}$$

The vector $\mathbf{U}_{h,i}^k(t)$ denotes the unknown degrees of freedom of the solution that are advanced in time, and S_i is the boundary of V_i. Adopting a smooth test function from the same space of the basis function, thus $\psi_i^k(\mathbf{x}) = \phi_i^k(\mathbf{x})$, the DG formulation for each element i is given by:

$$\sum_{k=0}^{K} \left(\int_{V_i} \phi_i^k(\mathbf{x}) \phi_i^b(\mathbf{x}) dV \right) \frac{d\mathbf{U}_{h,i}^k}{dt} = \int_{V_i} \nabla \phi_i^b(\mathbf{x}) \cdot \mathbf{F}(\mathbf{U}_i(\mathbf{x})) dV - \oint_{S_i} \phi_i^b(\mathbf{x}) \mathbf{F}(\mathbf{U}_i(\mathbf{x})) \cdot \mathbf{n} dS. \tag{4}$$

DG schemes are compact and enable higher-order spatial discretisations by simply increasing the order of the polynomial representing the solution, thus avoiding any reconstruction and bringing advantages in applications concerning complex, unstructured meshes, as well as in scalability and parallel computing efficiency. However, the increased number of degrees of freedom evolved at each time step comes with an increased level of computational effort. The number of DOFs K depends upon the degree of the polynomial r and the spatial dimension d. For example, for modal bases on arbitrary shapes, the number of DOFs can be calculated from the following expression:

$$K(r, d) = \frac{1}{d!} \prod_{l=1}^{d} (r + l). \tag{5}$$

It can be realised that the number of DOFs increases exponentially as the order is increased, with a considerable growth in computational costs, especially for 3-dimensional problems.

Traditionally, the basis can be represented through Lagrange Finite Element or node-based bases. With such a choice the DOFs to be solved are the node variables, at the vertices for a linear reconstruction, for example. In this work a modal

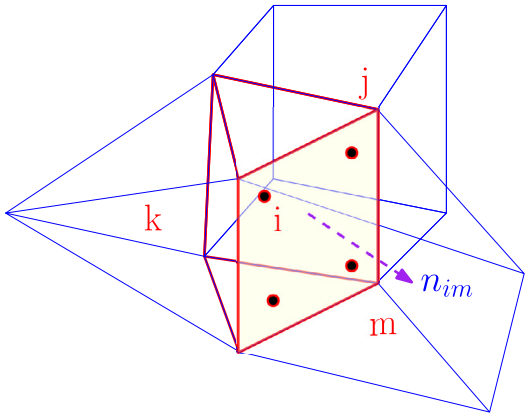

Fig. 1. Drawing illustrating a typical arrangement for a considered cell i and some its direct side neighbours m.

formulation is used, which allows for the same basis to be used for any element shape and avoids the underintegration errors often present in nodal implementations. In the modal formulation, the unknowns to be solved are the polynomial expansion coefficients, and a popular choice for the polynomial basis functions is the cell centred Taylor series expansion [33–36], as follows:

$$\phi_i^k(\mathbf{x})|_{V_i} = \frac{(x-x_{c_i})^{p_k}}{h_i^{p_k}} \frac{(y-y_{c_i})^{q_k}}{h_i^{q_k}} \frac{(z-z_{c_i})^{r_k}}{h_i^{r_k}} - \frac{1}{|V_i|} \int_{V_i} \frac{(x-x_{c_i})^{p_k}}{h_i^{p_k}} \frac{(y-y_{c_i})^{q_k}}{h_i^{q_k}} \frac{(z-z_{c_i})^{r_k}}{h_i^{r_k}} dV\,, \tag{6}$$

where $0 \leq p_k + q_k + r_k \leq r$. The index i ranges over the total number of elements, and $x_{c_i}, y_{c_i}, z_{c_i}$ are the coordinates of the cell centre of the considered element i. The basis functions are intentionally designed such that the higher-order modes vanish when integrating within the considered cell i, which is convenient when pursuing conservation and seamless interaction between DG and FV. Of great importance is the normalization of the basis function with a coefficient h, in this work taken as the square root of target cell's volume, used to improve the mass matrix conditioning, without which in the present study we could not achieve higher than 4^{th} of accuracy for the meshes and test problems attempted, a finding that might merit further investigation in the future.

We have resorted to these basis functions since we want to be able to handle arbitrary unstructured meshes and element shapes, and therefore the integration of the basis functions in physical space requires the decomposition of elements into triangles or tetrahedrals. This strategy has been previously documented in other studies [35–38], and the resulting mass matrix for each cell is given by:

$$M_{bk} = \int_{V_i} \phi_i^b(\mathbf{x}) \phi_i^k(\mathbf{x}) dV\,, \qquad \text{with } b = 0, 1, .., K \text{ and } k = 0, 1, .., K\,. \tag{7}$$

The non-uniquely defined intercell fluxes in Eq. (4) are determined in the same manner as in the FV framework, i.e. with an exact or approximate Riemann solver [3]. The semi-discrete system can be written as:

$$M_{bk} \frac{d\mathbf{U}_{h,i}^k}{dt} = \sum_{g=1}^{N_v} \omega_g \mathbf{F}(\mathbf{U}_i(\mathbf{x}_{i,g})) \cdot \nabla \phi_i^b(\mathbf{x}_{i,g}) |V_i| - \sum_{h=1}^{N_f} \sum_{\alpha=1}^{N_{qp}} \tilde{F}^{\mathbf{n_{im}}} \left(\mathbf{U}_{im,L}^n(\mathbf{x}_{im,\alpha}, t), \mathbf{U}_{im,R}^n(\mathbf{x}_{im,\alpha}, t) \right) \omega_\alpha \cdot \phi_i^b |S_{im}|, \tag{8}$$

where $\tilde{F}^{\mathbf{n_{im}}}$ is the numerical flux normal to the interface between cell i and cell m as shown in Fig. 1. N_f is the number of faces, N_v is the number of the volume Gaussian quadrature points, N_{qp} is the number of face quadrature points, and $|S_{im}|$ is the surface area of the considered face. $\mathbf{U}_{im,L}^n(\mathbf{x}_{im,\alpha}, t)$ and $\mathbf{U}_{im,R}^n(\mathbf{x}_{im,\alpha}, t)$ are the discontinuous solutions for cell i and cell m at the prescribed face Gaussian quadrature points respectively; while $\mathbf{x}_{im,\alpha}$ and ω_α, and $\mathbf{x}_{i,g}$ and ω_g correspond to different face and volume Gaussian integration points and weights respectively.

The Eq. (8) can be written as:

$$\mathbf{M}_i \frac{d\mathbf{U}_i}{dt} + \mathbf{R}_i(\mathbf{U}_i) = 0, \tag{9}$$

where $\mathbf{U}_i$ is the approximate solution, $\mathbf{M}_i$ is the mass matrix and $\mathbf{R}_i(\mathbf{U}_i)$ is the residual vector.

2.2. Finite volume method

Consider the same unsteady non-linear hyperbolic system of conservation laws of Eq. (1) in the same physical domain consisting of the same element types. Integrating Eq. (1) over a considered cell element i using a high-order explicit finite-volume formulation the following equation is obtained:

$$\frac{d\overline{\mathbf{U}}_i}{dt} = -\frac{1}{|V_i|}\sum_{j=1}^{N_f}\sum_{\alpha=1}^{N_{qp}} \tilde{F}^{\mathbf{n_{ij}}}\left(\mathbf{U}^n_{ij,L}(\mathbf{x}_{ij,\alpha},t), \mathbf{U}^n_{ij,R}(\mathbf{x}_{ij,\alpha},t)\right)\omega_\alpha |S_{ij}|, \tag{10}$$

where $\overline{\mathbf{U}}_i$ are the volume averaged conserved variables

$$\overline{\mathbf{U}}_i = \frac{1}{|V_i|}\int_{V_i} \mathbf{U}(\mathbf{x})\, dV, \tag{11}$$

and $F^{\mathbf{n_{ij}}}$ is the numerical flux normal to the cell interface between cell i and one of its neighbouring cells j, N_f being the number of faces of the considered cell, N_{qp} is the number of quadrature points at the considered face, and $|S_{ij}|$ is the surface area of the corresponding face. $\mathbf{U}^n_{ij,L}(\mathbf{x}_{ij,\alpha},t)$ and $\mathbf{U}^n_{ij,R}(\mathbf{x}_{ij,\alpha},t)$ are high-order approximations of the solutions for cell i and cell j respectively; while α corresponds to different Gaussian integration points $\mathbf{x}_\alpha$ and weights ω_α over each face, coincident with the ones defined for the surface integral in the DG formulation.

2.2.1. Reconstruction

In the present FV implementation, high-order accuracy is achieved through a reconstruction process, where for each cell i we build an order r polynomial $p_i(\mathbf{x})$ that can provide $r+1$ order of accuracy. One of the key requirements is that the reconstruction polynomial, when integrated within the considered cell, should have the same value as the volume average of a general quantity $\mathbf{U}_i$:

$$\overline{\mathbf{U}}_i = \frac{1}{|V_i|}\int_{V_i} p_i(\mathbf{x})\, dV. \tag{12}$$

The present polynomial reconstruction is primarily based on the approaches of [37–41], that have been applied to a wide-range of flow problems including laminar, transitional and turbulent flows at a wide spectrum of Mach numbers [28,30–32,37,38,40–58] and only the key ingredients will be detailed in this work. What is different from the previous approaches [37–41] is that we no longer employ any transformation from physical space to reference space to reduce scaling effects, but we solve the reconstruction problem in the physical space. A stencil is built to perform the reconstruction by adding M neighbouring cells to our considered element i. We use the stencil based compact algorithm (SBC) as defined in [55] where $M = 2K$ for ensuring that we have an overdetermined least square system which was found to be robust for arbitrary unstructured meshes [26,27,39,55,59–61]. The central stencil $\mathcal{S}^1$ is given by:

$$\mathcal{S}^c_i = \bigcup_{m=0}^{M_c} V_m, \tag{13}$$

where the index m refers to the local numbering of the elements in the stencil. Index 0 corresponding to the considered element i, and index c refers to the stencil number ($c = 1$ for the central stencil). The r^{th} order reconstruction polynomial is an expansion over the previously introduced Taylor basis $\phi_k(\mathbf{x})$ for the DG method in Eq. (6), and is given by:

$$p(\mathbf{x}) = \sum_{k=0}^{K} a_k\phi_k(\mathbf{x}) = \mathbf{U}_0 + \sum_{k=1}^{K} a_k\phi_k(\mathbf{x}), \tag{14}$$

where $\mathbf{U}_0$ refers to the conserved variables vector of cell i, and a_k are the degrees of freedom of the polynomial. The degrees of freedom a_k for each cell m satisfy the condition that the volume average of the reconstruction polynomial $p(\mathbf{x})$ is equal to the cell average of the solution $\mathbf{U}_m$:

$$\int_{V_m} p(\mathbf{x})\, d\mathbf{x} = |V_m|\overline{\mathbf{U}}_0 + \sum_{k=1}^{K}\int_{V_m} a_k\phi_k\, d\mathbf{x} = |V_m|\overline{\mathbf{U}}_m, \quad m = 1,\ldots,M. \tag{15}$$

This condition is satisfied also due to the Taylor basis functions selected. Defining the following quantities:

$$A_{mk} \equiv \int_{V_m} \phi_k\, dxdydz, \quad b_m \equiv |V_m|(\overline{\mathbf{U}}_m - \overline{\mathbf{U}}_0), \tag{16}$$

Eq. (15) can be rearranged in a matrix form as:

$$\sum_{k=1}^{K} A_{mk} a_k = b_m, \quad m = 1, 2, \ldots M. \tag{17}$$

The overdetermined least-squares system is solved by a QR decomposition [62] and for speeding up the computation we pre-store the Moore-Penrose pseudo-inverse of A_{mk} as documented in [55].

2.2.2. CWENOZ scheme

For the CWENOZ scheme, we combine an optimal (high-order) polynomial p_{opt} that relies on the central stencil with linear polynomials using the compact directional stencils. In regions where the variation of the solution is smooth, the desired order of accuracy can be achieved, while the reconstruction is mostly influenced by the lower-order polynomials with the smoothest variation of the solution when the solution is discontinuous. For the directional stencils, we use the definition noted as Type3 as introduced in [55]. The definition of the optimal polynomial is given by:

$$p_{opt}(\mathbf{x}) = \sum_{s=1}^{s_t} \lambda_s p_s(\mathbf{x}), \tag{18}$$

where s is the stencil index, with $s = 1$ being assigned to the central stencil and s_t being the total number of stencils, and λ_s being the linear coefficients for each stencil that are required to have a sum of 1. The p_1 polynomial is obtained by subtracting the lower-order polynomials from the optimum polynomial as follows:

$$p_1(\mathbf{x}) = \frac{1}{\lambda_1}\left(p_{opt}(\mathbf{x}) - \sum_{s=2}^{s_t} \lambda_s p_s(\mathbf{x})\right). \tag{19}$$

The CWENOZ reconstruction polynomial is obtained by combining all the polynomials non-linearly as follows:

$$p(\mathbf{x})^{\text{cwenoz}} = \sum_{s=1}^{s_t} \omega_s p_s(\mathbf{x}), \tag{20}$$

with ω_s being the non-linear weights for each polynomial. The final reconstructed polynomial is given by the following expression:

$$p(\mathbf{x})^{\text{cwenoz}} = \mathbf{U}_0 + \sum_{k=1}^{K} \tilde{a}_k \phi_k(\mathbf{x}), \tag{21}$$

where $\tilde{a}_k$ are the CWENOZ reconstructed degrees of freedom. When the solution is smooth $\omega_s \approx \lambda_s$ the optimum polynomial is recovered. The non-linear weight ω_s is defined as:

$$\omega_s = \frac{\tilde{\omega}_s}{\sum_{s=1}^{s_t} \tilde{\omega}_s} \quad \text{where} \quad \tilde{\omega}_s = \lambda_s\left(1 + \frac{\tau}{\epsilon + \mathcal{SI}_s}\right), \tag{22}$$

with τ being the universal oscillation indicator and taken as the absolute difference between the smoothness indicators as follows:

$$\tau = \left(\frac{\sum_{s=2}^{s_t} |\mathcal{SI}_s - \mathcal{SI}_1|}{s_t - 1}\right)^b. \tag{23}$$

For this study we use $\epsilon = 10^{-14}$ and $b = 4$. Firstly we assign a large value for the non-normalised linear weight for the central stencil λ_1', and then normalising it as:

$$\lambda_1 = 1 - \frac{1}{\lambda_1'}, \tag{24}$$

while all the linear weights of the lower-order polynomials have the same value and are calculated by

$$\lambda_s = \frac{1 - \lambda_1}{s_t - 1}. \tag{25}$$

We use the following smoothness indicator $\mathcal{SI}_s$ which is given by:

$$\mathcal{SI}_s = \sum_{1\leq|\beta|\leq r}\int_{V_0}\left(\mathcal{D}^\beta p_s(x,y,z)\right)^2(dx,dy,dz), \tag{26}$$

where $\mathcal{D}$ is the derivative operator, β is a multi-index and r is the polynomial's order. Since the smoothness indicator is a quadratic function of the degrees of freedom (a_k^s) it can be rewritten as:

$$\mathcal{SI}_s = \sum_{k=1}^{K} a_k^s \left(\sum_{q=1}^{K}\mathcal{OI}_{kq}a_q^s\right), \tag{27}$$

having defined the oscillation indication matrix $\mathcal{OI}_{kq}$ as:

$$\mathcal{OI}_{kq} = \sum_{1\leq|\beta|\leq r}\int_{V_0}\left(\mathcal{D}^\beta\phi_k(x,y,z)\right)\left(\mathcal{D}^\beta\phi_q(x,y,z)\right)(dx,dy,dz), \tag{28}$$

which is precomputed and stored at the beginning of the simulation. It needs to be stressed that for the CWENOZ variant employed in this study a large value is assigned to the non-normalised linear weight corresponding to the central stencil $\lambda_1' > 10^3$. Previous sensitivity studies on this variant have concluded that a high-value is required to achieve the desired order of accuracy and the reader is referred to the work of Tsoutsanis and Dumbser [40] for additional information.

2.3. Fluxes & time advancement

The flux approximation and temporal discretisation techniques are shared between the FV and DG methods. For the inviscid fluxes, the approximate HLLC (Harten-Lax-van Leer-Contact) Riemann solver of Toro [63] is employed, unless otherwise stated. The solution is advanced in time by a third-order TVD Runge-Kutta method:

$$\mathbf{U}_i^{(n+1/3)} = \mathbf{U}_i^n + \Delta t M^{-1} R_i(\mathbf{U}), \tag{29}$$

$$\mathbf{U}_i^{n+2/3} = \frac{3}{4}\mathbf{U}_i^n + \frac{1}{4}\mathbf{U}_i^{(n+1/3)} + \frac{1}{4}\Delta t M^{-1} R_i(\mathbf{U}^{(n+1/3)}), \tag{30}$$

$$\mathbf{U}_i^{n+1} = \frac{1}{3}\mathbf{U}_i^n + \frac{2}{3}\mathbf{U}_i^{(n+2/3)} + \frac{2}{3}\Delta t M^{-1} R_i(\mathbf{U}^{(n+2/3)}), \tag{31}$$

and the time step Δt is selected according to:

$$\Delta t = \mathrm{CFL}\frac{1}{2r+1}\min_i\left(\frac{h_i}{S_i}\right), \tag{32}$$

where S_i is an estimate of the maximum in absolute value of the propagation speed in the cell V_i, h_i is a characteristic length of the element V_i and CFL refers to the Courant-Friedrichs-Lewy condition.

All the volume/surface/line integrals are approximated by Gaussian quadrature rule suitable for the order of polynomial employed [64]. All the schemes developed are implemented in the `UCNS3D` CFD code [32] which is written in object-oriented Fortran 2003, employing MPI message passing interface (MPI), and the Open Multi-Processing (OpenMP) application programming interface (API), and the reader is referred to [51,65] for more details on implementation and performance benchmarks. The computational times reported in each case are obtained for the same hardware (and compilation settings) and normalised with respect to a reference setup for the same hardware so that the performance of various algorithms under identical hardware can be appreciated.

2.4. Hybrid DG-FV

The operations performed by the modified version of the `UCNS3D` code, and used for the present study, are summarized in the flow chart in Fig. 2. As already mentioned, the `UCNS3D` code is originally a pure FV code. Hence, the implementation of a modal DG scheme allows the hybridisation of the two frameworks, where the unlimited DG solution is checked at every RK stage of each time step, and the underlying FV type reconstruction is enabled in the cells that are deemed troubled by the solution checking criteria. For the troubled cells only, the reconstructed polynomial is substituted into the DG solution as follows:

$$\mathbf{U}_i(\mathbf{x},t) = \mathbf{U}_0 + \sum_{k=1}^{K}\mathbf{U}_{h,i}^k(t)\phi_i^k(\mathbf{x}) = \mathbf{U}_0 + \sum_{k=1}^{K}\tilde{a}_k\phi_k(\mathbf{x}), \tag{33}$$

where the first degree of freedom assigned with index $j,k=0$ ensures conservation, since the higher-order terms $j,k=1,2,..,K$ cancel out when integrated within the considered cell due to the employed basis. Since the same basis is used for both DG and FV we simply set $U^{j}_{h,i}=\tilde{a}_k$, where $\tilde{a}_k$ are the CWENOZ reconstructed polynomial coefficients as defined in Sec. 2.2.2. It has to be remarked that the strategy adopted in this work, where the solution in the troubled cells is provided by a CWENOZ reconstruction, is designed following efficiency and robustness arguments. The CWENOZ reconstruction, presented in the UCNS3D environment in [40], demonstrated a consistent improvement in terms of computational efficiency over the classic WENO scheme, as well as insensitivity to the magnitude of the linear weight of the central stencil with respect to the CWENO scheme. However, merely applying any type of WENO reconstruction on the troubled cells will cause loss of information provided by the DG solution at the subcell level, since the reconstruction operates on the cell averages of the neighbouring cells. For this reason, limiters operating on the subcell level were designed in [66–68]. The idea is to use either a first order FV scheme or a FV type reconstruction on the subgrid obtained from the *decomposition* of the troubled cells. The number of subcells is calculated based on the desired accuracy while maximizing the allowed CFL number. This method is clearly able to preserve more accurately the features provided by the DG scheme and is attractive and fairly affordable on uniform meshes. However, the procedure is not as straightforward when applied to unstructured meshes and seems problematic for meshes composed of arbitrary elements and for those meshes with transition layers and/or bad quality elements. If the subcell subdivision can not be performed optimally, it can also have an adverse impact on the already restrictive time step size of the DG method. Recent developments [36,69] have demonstrated that it can be applied to Voronoi type of meshes therefore encouraging further work to expand it to meshes including low-quality of cells.

The readily available reconstruction stencil provided by the underlying FV scheme of the UCNS3D solver, allows for different configurations of the bounds definition of the troubled cell detection to be tested. As will be shown later, extension of the bounds to the whole stencil reduces the number of troubled cells, especially in smooth flow regions.

The troubled cell indicators will also be tested with two different flagging procedures. In *case1*, the solution is checked at every RK stage, thus troubled cells are allowed to change their condition within the same time step at different RK stages, while in *case2*, cells that are deemed invalid at the first stage cannot change their status until the next time step.

Because WENO type reconstructions are still prone to some oscillations, increasingly so for higher orders, additional solution checks are performed on the reconstructed solution. In particular, we check that the pressure and density remains positive through the reconstruction, while also employing the condition of Harten et al. [11], where the FV reconstructed values of density and pressure for each Gaussian quadrature points (α) at all cell interfaces l must satisfy the following:

$$|\rho_{il,\alpha}-\rho_i|<0.8\rho_i \;\text{ and }\; |p_{il,\alpha}-p_i|<0.8p_i. \tag{34}$$

If this condition (34) is not satisfied for any Gaussian quadrature point, we switch to a 2nd-order MUSCL scheme or a 1st-order upwind Godunov scheme, something that can have a detrimental impact on the accuracy of the framework for that cell but might be required for robustness as usually deployed in MOOD framework [28,29]. The activation of this switch has not been encountered for the problems attempted herein but the reader is referred to the work of Tsoutsanis et al. [29] where the switch is activated for test problems such as shock-induced collapse of bubbles in multicomponent applications and is needed since otherwise the simulation would have blown-up.

2.5. Troubled cell indicators

The switch for each element from a DG solution to the CWENOZ one is governed by a troubled cell indicator, the design of which is nontrivial and for a comparison of the most popular indicators we refer to [70]. Assuming that the reconstruction procedure activated in the troubled region does not deteriorate the original order of convergence, the importance of an efficient detector is more aimed at reducing computational costs, avoiding unnecessary reconstruction in smooth flow regions. In this work, we will test a shock detector type and a class of MOOD type detectors, with limited and extend bounds as described in Appendix A, in order to assess the impact of the FV type reconstruction on the computational time and general accuracy. The adopted indicators are now briefly introduced:

Shock Detector type indicator: Our implementation of the shock detector is similar to the KXRCF indicator [23], which was built upon the convergence properties of the DG method at outflow boundaries, thus evaluating the solution jump across neighbouring elements, that is greater in the presence of discontinuities, normalising with respect to the average convergence rate and scaling with respect to a characteristic cell length.

As pointed out in [24], due to the presence of a small scaling parameter, this detector is often too sensitive and in [24], a modification using the jumps in cell-averaged solutions between the target cell and all its neighbours as a measure of the discontinuity, was proposed. In our work we use a detector similar to the one introduced in [24], where the solution of the neighbouring cells is cell-averaged over the respective cell and not over the target cell. This results in the following:

$$\frac{\sum_{n=1}^{N}|\frac{1}{V_0}\int_{V_0}U_0(\mathbf{x})dV-\frac{1}{V_n}\int_{V_n}U_n(\mathbf{x}))dV|}{\max_{n\in\{0...N\}}\{\frac{1}{V_n}|\int_{V_n}U_n(\mathbf{x})dV|\}}>C_k, \tag{35}$$

where the threshold value C_k is usually taken to be unity unless otherwise specified.

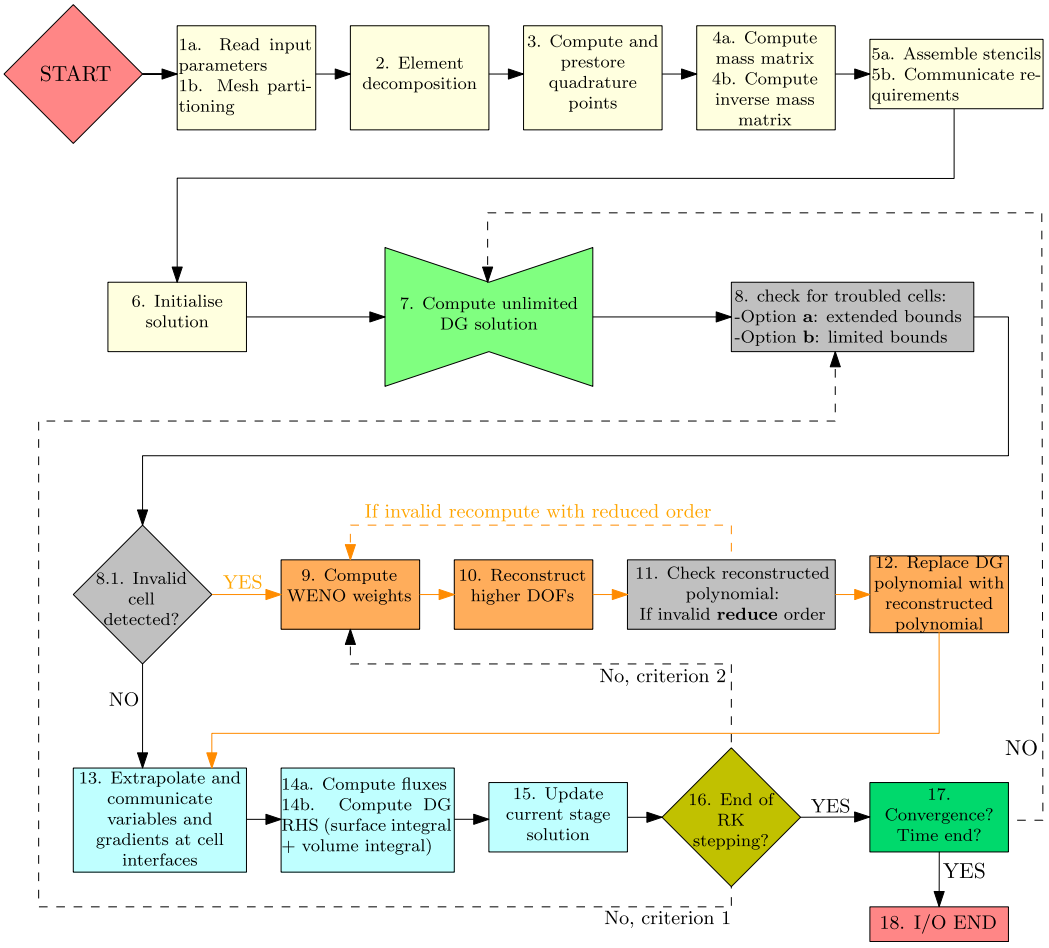

Fig. 2. Flow chart for the implementation of the DG method in the UCNS3D code, modified from the pure FV implementation as presented in [51]. The light yellow label refers to the pre-stored operations, performed only once at the beginning of the simulation. The troubled cell detection steps are coloured in grey and the orange label refers to FV type non-linear reconstruction. Flux calculation and time stages are labelled in light blue. (For interpretation of the colours in the figure(s), the reader is referred to the web version of this article.)

MOOD type indicator: In this work we adopt two criteria, often used within the MOOD paradigm [26,27,66,67], namely the Physical Admissible Detector (PAD) and Numerical Admissible Detector (NAD) [27]. The PAD checks for negative or NaN solutions for the density and pressure variables, which are unphysical, while the NAD checks that the solution is monotonic and that new extrema are not created according to the discrete maximum principle (DMP). The main difference to the original implementation within the MOOD framework, i.e. using the PAD and NAD in *a priori* fashion, is that the neighbouring solutions are compared with the target cell solution at the same time level.

The NAD criteria used in this work refer to the DMP-relaxed margins proposed in [28]:

$$\min_{y\in\mathcal{V}_i}(U^n(y)) - \delta \leq U(x) \leq \max_{y\in\mathcal{V}_i}(U^n(y)) + \delta, \tag{36}$$

and the margin δ is defined as:

$$\delta = \max(10^{-4}, \alpha \cdot [\max_{y\in\mathcal{V}_i}(U^n(y)) - \min_{y\in\mathcal{V}_i}(U^n(y))]). \tag{37}$$

The choice of the parameter α is ruled by the degree of oscillations admitted in the solution. In this work the values of $\alpha = 10^{-3}$ as suggested in [71] and $\alpha = 10^{-1}$ as used in the relaxed version of [40] are employed. When using the former value, the detector will be labelled as MOOD^O, and MOOD^R when using the latter value.

We remark that, when Euler equations are considered, the quantities checked by both the shock detector and MOOD type indicators presented above, are density and energy only.

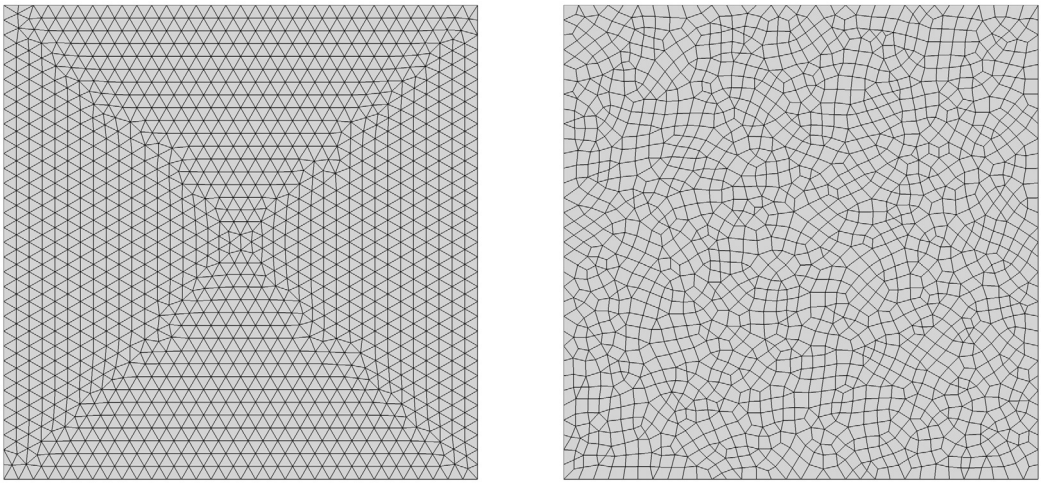

(a) Triangular mesh (b) Hybrid mesh

Fig. 3. Unstructured mesh samples with 32 edges per side.

3. Applications

A large number of test cases of increasing complexity have been selected to assess the performance of the numerical frameworks, starting from a comparison of the convergence order and computational cost of the FV, DG, and hybrid methods for smooth profiles, the non-oscillatory properties in the advection of discontinuous profiles, and concluding with an assessment of the hybrid DG-FV schemes with various troubled cell indicators for the solution of the Euler equations for compressible, inviscid flow. The list of test cases is as follows:

- 2D Vortex Evolution. This test problem provides an assessment of the accuracy and computational footprint of the methods applied on the Euler equations.
- 2D Solid Body Rotation. This test problem is ideal for assessing simultaneously the accuracy and non-oscillatory behaviour of the schemes. We use this problem to show the effects of different set up for the MOOD type troubled cell indicator at different polynomial orders.
- Shu-Osher Problem. This test problem provides an assessment of the non-oscillatory properties of the methods in combination with smooth flow features and is used to evaluate different typologies of detectors.
- Double Mach reflection. This test problem provides an assessment of the non-oscillatory properties of the hybrid scheme with different detectors in presence of strong and secondary shock waves.
- Schardin's Problem. This test problem is used to assess the performance of the scheme in a flow problem characterised by the presence of strong gradients and regions interacting with vortices.
- 3D inviscid subsonic Taylor-Green Vortex. A well-established test problem for assessing the performance of the schemes in an under-resolved flow setting.
- 3D inviscid supersonic Taylor-Green Vortex. A new variation of the Taylor-Green vortex to simultaneously examine the non-oscillatory properties of the schemes.
- 3D sonic boom prediction of the Lockheed Martin 1021-01. A well-established test problem for predicting the acoustic footprint of a supersonic aircraft.

Additional test cases are provided in Appendix B and Appendix C, where the hybrid scheme is calibrated and tested on different mesh types for the scalar advection of smooth and discontinuous profiles respectively.

3.1. 2D vortex evolution

A popular test case for testing the accuracy of the schemes in the context of unsteady inviscid Euler equations is the one introduced by Balsara and Shu [72], and involves the propagation of an isentropic vortex at a supersonic Mach number across a 2D domain at a 45° direction. The computational domain is given by $[0, 10] \times [0, 10]$ with periodic boundary conditions applied on all sides. We have performed the calculations on the triangular and hybrid unstructured grids illustrated in Fig. 3, and on uniform mesh, with four different resolutions corresponding to 16, 32, 64 and 128 edges per side for $\mathcal{P}2$ and $\mathcal{P}3$, and 8, 16, 32 and 64 edges for $\mathcal{P}4$ discretisation. The domain is initially unperturbed with condition $(\rho, u, v, p) = (1, 1, 1, 1)$, while the vortex perturbations, of radius r, are given by:

Table 1
Values for e_{L^∞} and e_{L^2} error norms and convergence rates for pure FV and DG framework, and hybrid DG-FV with the MOOD^O for the 2D Vortex evolution test case. For the hybrid schemes the average percentage of troubled cells is averaged on the total number of time steps and the additional costs for the reconstruction in the troubled cells is quantified though the CPU coefficient normalised with the pure DG computational time on the same mesh and polynomial order.

Order/Number of Edges	FV				DG				DG/MOOD					
Quadrilateral Mesh	e_{L^∞}	$\mathcal{O}_{L^\infty}$	e_{L^2}	$\mathcal{O}_{L^2}$	e_{L^∞}	$\mathcal{O}_{L^\infty}$	e_{L^2}	$\mathcal{O}_{L^2}$	e_{L^∞}	$\mathcal{O}_{L^\infty}$	e_{L^2}	$\mathcal{O}_{L^2}$	% troub. cells	CPU
$\mathcal{P}2/16$	3.08E-01	-	4.55E-02	-	6.20E-03	-	1.27E-03	-	2.60E-01	-	3.73E-02	-	42.1	1.41
$\mathcal{P}2/32$	1.54E-01	1.00	1.90E-02	1.26	4.43E-04	3.81	8.61E-05	3.88	3.72E-02	2.80	4.60E-03	3.02	15.9	1.27
$\mathcal{P}2/64$	2.86E-02	2.43	3.89E-03	2.29	2.19E-05	4.34	3.60E-06	4.58	3.09E-03	3.59	3.97E-04	3.54	0.71	1.03
$\mathcal{P}2/128$	4.31E-03	2.73	6.48E-04	2.58	8.89E-07	4.62	1.21E-07	4.89	2.23E-04	3.79	2.10E-05	4.24	0.16	1.06
$\mathcal{P}3/16$	2.18E-01	-	2.97E-02	-	5.13E-04	-	1.09E-04	-	1.68E-01	-	2.35E-02	-	42.4	1.26
$\mathcal{P}3/32$	3.89E-02	2.48	5.16E-03	2.52	1.67E-05	4.94	2.29E-06	5.57	2.88E-02	2.55	2.17E-03	3.44	7.35	1.08
$\mathcal{P}3/64$	8.63E-03	2.17	8.50E-04	2.60	2.84E-07	5.88	3.15E-08	6.18	1.22E-03	4.56	7.49E-05	4.86	0.70	1.05
$\mathcal{P}3/128$	5.54E-04	3.96	5.83E-05	3.87	1.03E-08	4.79	8.64E-10	5.19	6.03E-05	4.34	1.48E-06	5.66	0.16	1.02
$\mathcal{P}4/8$	5.77E-01	-	7.64E-02	-	9.83E-04	-	2.97E-04	-	6.83E-01	-	7.83E-02	-	45.7	1.29
$\mathcal{P}4/16$	2.30E-01	1.33	3.13E-02	1.29	6.99E-05	3.81	1.12E-05	4.73	2.18E-01	1.65	3.00E-02	1.38	34.3	1.21
$\mathcal{P}4/32$	3.83E-02	2.58	5.15E-03	2.60	5.63E-07	6.69	8.78E-08	7.00	3.04E-02	2.85	2.62E-03	3.52	7.36	1.07
$\mathcal{P}4/64$	8.11E-03	2.24	7.20E-04	2.84	7.54E-09	6.22	1.14E-09	6.27	1.69E-03	4.17	1.25E-04	4.39	0.72	1.05
Triangular Mesh	e_{L^∞}	$\mathcal{O}_{L^\infty}$	e_{L^2}	$\mathcal{O}_{L^2}$	e_{L^∞}	$\mathcal{O}_{L^\infty}$	e_{L^2}	$\mathcal{O}_{L^2}$	e_{L^∞}	$\mathcal{O}_{L^\infty}$	e_{L^2}	$\mathcal{O}_{L^2}$	% troub. cells	CPU
$\mathcal{P}2/16$	1.83E-01	-	2.26E-02	-	1.99E-03	-	2.73E-04	-	1.03E-01	-	1.27E-02	-	29.1	1.54
$\mathcal{P}2/32$	3.48E-02	2.40	5.06E-03	2.16	1.23E-04	4.02	1.68E-05	4.02	7.91E-03	3.71	9.54E-04	3.74	2.73	1.21
$\mathcal{P}2/64$	6.09E-03	2.51	9.27E-04	2.45	1.83E-05	2.75	1.16E-06	3.86	6.87E-04	3.52	6.79E-05	3.81	0.37	1.12
$\mathcal{P}2/128$	7.86E-04	2.95	1.26E-04	2.88	2.60E-06	2.81	1.57E-07	2.88	5.61E-05	3.62	4.07E-06	4.06	0.08	1.01
$\mathcal{P}3/16$	3.56E-02	-	5.36E-03	-	1.09E-04	-	1.64E-05	-	2.81E-02	-	3.86E-03	-	22.6	1.56
$\mathcal{P}3/32$	9.40E-03	1.92	8.55E-04	2.65	3.70E-06	4.88	6.43E-07	4.67	6.19E-03	2.18	3.77E-04	3.36	2.81	1.09
$\mathcal{P}3/64$	3.94E-04	4.58	4.83E-05	4.15	4.14E-07	3.16	3.34E-08	4.27	2.81E-04	4.46	2.19E-05	4.11	0.34	1.04
$\mathcal{P}3/128$	2.74E-05	3.85	3.04E-06	3.99	5.47E-08	2.92	2.48E-09	3.75	2.74E-05	3.36	8.24E-07	4.73	0.08	1.01
$\mathcal{P}4/8$	2.67E-01	-	3.68E-02	-	2.96E-04	-	6.59E-05	-	2.72E-01	-	3.77E-02	-	36.3	1.41
$\mathcal{P}4/16$	5.13E-02	2.38	6.73E-03	2.45	9.12E-06	5.02	1.49E-06	5.47	3.63E-02	2.91	4.46E-03	3.08	15.6	1.48
$\mathcal{P}4/32$	1.56E-02	1.72	1.29E-03	2.38	2.69E-07	5.08	4.49E-08	5.05	4.31E-03	3.08	3.16E-04	3.82	1.44	1.06
$\mathcal{P}4/64$	4.22E-04	5.20	6.88E-05	4.23	1.23E-08	4.45	1.10E-09	5.35	1.19E-04	5.18	7.54E-06	5.39	0.35	1.04
Hybrid Mesh	e_{L^∞}	$\mathcal{O}_{L^\infty}$	e_{L^2}	$\mathcal{O}_{L^2}$	e_{L^∞}	$\mathcal{O}_{L^\infty}$	e_{L^2}	$\mathcal{O}_{L^2}$	e_{L^∞}	$\mathcal{O}_{L^\infty}$	e_{L^2}	$\mathcal{O}_{L^2}$	% troub. cells	CPU
$\mathcal{P}2/16$	2.82E-01	-	3.62E-02	-	6.07E-03	-	8.51E-04	-	2.24E-01	-	2.77E-02	-	26.3	1.46
$\mathcal{P}2/32$	7.66E-02	1.88	1.01E-02	1.84	4.30E-04	3.82	5.77E-05	3.88	2.00E-02	3.49	2.22E-03	3.64	5.10	1.20
$\mathcal{P}2/64$	1.27E-02	2.60	1.88E-03	2.42	4.71E-05	3.19	5.25E-06	3.46	1.37E-03	3.87	1.73E-04	3.69	0.41	1.13
$\mathcal{P}2/128$	1.89E-03	2.74	2.77E-04	2.76	4.96E-06	3.25	6.82E-07	2.94	1.17E-04	3.54	9.54E-06	4.18	0.09	1.03
$\mathcal{P}3/16$	1.04E-01	-	1.36E-02	-	5.93E-04	-	7.69E-05	-	8.34E-02	-	1.03E-02	-	27.4	1.29
$\mathcal{P}3/32$	2.93E-02	1.82	2.45E-03	2.48	2.03E-05	4.87	3.32E-06	4.53	1.38E-02	2.60	9.51E-04	3.44	5.15	1.10
$\mathcal{P}3/64$	9.21E-04	4.99	1.49E-04	4.04	2.46E-06	3.05	1.86E-07	4.16	3.29E-04	5.39	3.83E-05	4.63	0.42	1.09
$\mathcal{P}3/128$	6.48E-05	3.83	7.44E-06	4.32	1.72E-07	3.84	1.24E-08	3.91	5.86E-05	2.49	1.58E-06	4.60	0.10	1.02
$\mathcal{P}4/8$	3.59E-01	-	4.50E-02	-	2.13E-03	-	3.30E-04	-	3.67E-01	-	4.62E-02	-	36.3	1.35
$\mathcal{P}4/16$	1.35E-01	1.41	1.63E-02	1.46	1.23E-04	4.11	1.55E-05	4.41	1.00E-01	1.88	1.19E-02	1.96	24.0	1.39
$\mathcal{P}4/32$	2.99E-02	2.17	2.70E-03	2.59	2.03E-06	5.93	2.75E-07	5.82	1.54E-02	2.70	9.67E-04	3.62	2.97	1.16
$\mathcal{P}4/64$	1.01E-03	4.89	1.60E-04	4.08	6.30E-08	5.01	7.12E-09	5.27	3.70E-04	5.38	2.19E-05	5.47	0.42	1.05

$$\delta T = -\frac{(\gamma-1)\epsilon^2}{8\gamma\pi^2}e^{(1-r^2)}, \qquad (\delta u, \delta v) = \frac{\epsilon}{2\pi}e^{0.5(1-r^2)}\left(-(y-5),(x-5)\right). \tag{38}$$

Temperature and density are defined as $T = p/\rho$, and $S = p/\rho^\gamma$. The vortex strength $\epsilon = 5$ and adiabatic gas constant $\gamma = 1.4$. The simulation is performed for 10 periods and the e_{L^2} and e_{L^∞} error are computed as follows, respectively:

$$e_{L^2} = \sqrt{\frac{\sum_i \int_{\Omega_i}\left(U_e\left(x,t_f\right) - U_c\left(x,t_f\right)\right)^2 dV}{\sum_i |\Omega_i|}}, \tag{39}$$

$$e_{L^\infty} = \mathcal{M}ax\left|\left(\mathbf{U}_e\left(x,t_f\right) - \mathbf{U}_c\left(x,t_f\right)\right|\right., \tag{40}$$

where $\mathbf{U}_c\left(x,t_f\right)$ and $\mathbf{U}_e\left(x,t_f\right)$ are the computed solution at final time $t = 10$, and the exact solutions given by the initial condition itself, respectively.

We adopted a value of CFL$= 0.5$ for the time step calculation, and a value of $\lambda_1 = 10^7$ for the CWENOZ reconstruction central stencil for this and the subsequent test cases, unless otherwise specified (we refer to [40] for a sensitivity analysis to the λ_1 value, it demonstrates the insensitivity to this parameter in the CWENOZ implementation). The results for this test case are presented in Table (1) and can be observed how the convergence order of the DG scheme is close to the theoretical one, whereas the FV scheme for the same polynomial order is able to achieve such convergence only for finer meshes, and would probably require a smaller CFL number, although this is out of scope for the present study. It is interesting to observe, however, how the sub-optimal order of convergence of the FV part affects the hybrid scheme, where the troubled cells are here determined by the MOOD type indicator. Similarly to the scalar advection test case, the indicator erroneously detects troubled cells in correspondence of the vortex core (see Fig. 4), and is of great impact for the coarser meshes. As the mesh

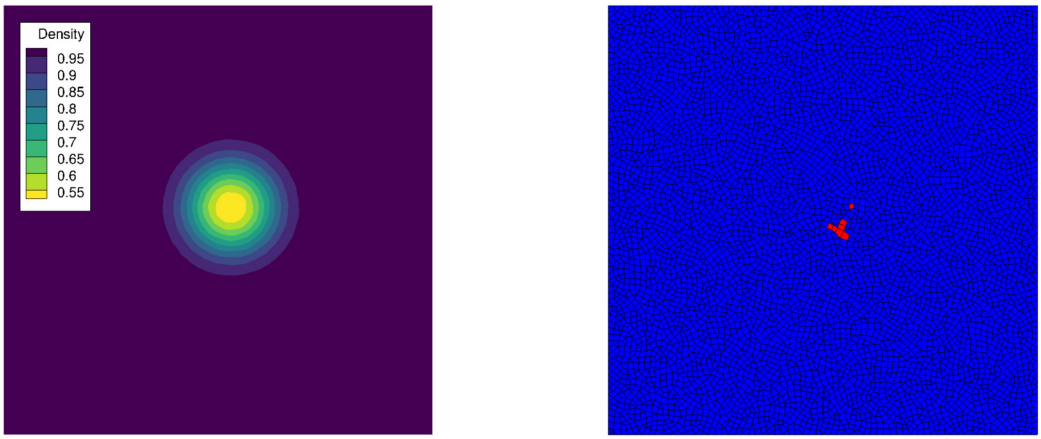

Fig. 4. Density contours (*left*) and troubled cell location (*right*) at initial time for the 2D vortex evolution test case for hybrid mesh with 64 edges per side. It can be noticed that the troubled cells are located in correspondence with the vortex core.

is refined, the average percentage of troubled cells is greatly reduced and the global accuracy is closer to the one obtained with a pure DG scheme. Similarly to the smooth scalar advection test case, we noticed an increase by 1.4-1.5 times in the computational time for situation with larger portions of troubled cells, and by 1.05 for finer meshes with less troubled cells.

3.2. 2D solid body rotation

The solid body rotation test of Leveque [73] is here considered to investigate the correct and accurate revolution of a slotted cylinder, smooth hump and sharp cone shapes, as a measure of the low-dissipativity and non-oscillatory properties of the hybrid scheme with CWENOZ reconstruction. The computational domain is again a $[0, 10] \times [0, 10]$ square with periodic boundaries at all sides as previously defined, and the following continuity equation is adopted:

$$\frac{\partial U}{\partial t} + \nabla \cdot (\mathbf{v}U) = 0. \tag{41}$$

The velocity $\mathbf{v}$ describing the revolution of the profile around the centre of the domain $(0.5, 0.5)$ is given by:

$$\mathbf{v}(x, y) = (0.5 - y, x - 0.5). \tag{42}$$

The smooth hump is centred at $(x_0 = 0.25, y_0 = 0.5)$, the sharp cone at $(x_0 = 0.5, y_0 = 0.25)$ and the slotted cylinder is centred at $(x_0 = 0.5, y_0 = 0.75)$, and are described by the following functions respectively:

$$\mathbf{f}(x, y) = \frac{1 + \cos(\pi r(x, y))}{4}, \tag{43}$$

$$\mathbf{f}(x, y) = 1 - r(x, y), \tag{44}$$

and

$$\mathbf{f}(x, y) = \begin{cases} 1, & \text{if } |x - x_0| \geq 0.025 \text{ or } y \geq 0.85 \\ 0, & \text{if otherwise.} \end{cases} \tag{45}$$

The normalised distance from the centres (x_0, y_0) is given by:

$$r(x, y) = (1/r_0)\sqrt{(x - x_0)^2 + (y - y_0)^2}, \tag{46}$$

with $r_0 = 0.15$ everywhere else in the domain, the solution is initialised with zero. The exact solution coincides with the initial solution, and the final solution is found after one full revolution $t_f = 2\pi$. The hybrid unstructured mesh composed of mixed quadrilateral and triangular elements is used, with 64 edges per side of the computational domain as shown in Fig. 3(b). The pure FV with CWENOZ reconstruction, and the hybrid DG-FV scheme with the MOOD type indicator with different threshold values and bounds definition, ranging from 3rd- to 5th-order of spatial accuracy are employed. Assuming a value of CFL= 0.5 for the calculation of the time step and of $\lambda_1 = 10^7$ for the linear weight of central stencil for CWENOZ reconstruction, the computations are performed for one full revolution $t_f = 2\pi$, and the final results are illustrated in Fig. 5. From Fig. 5 it can be noticed that all schemes captured the correct shapes with the pure FV scheme being, as expected, more dissipative. Some oscillations at the base of and at the edge of the slotted cylinder are found for all the accuracy order, as already reported in [40]. A higher accuracy is achieved with the hybrid scheme, and the oscillations are completely

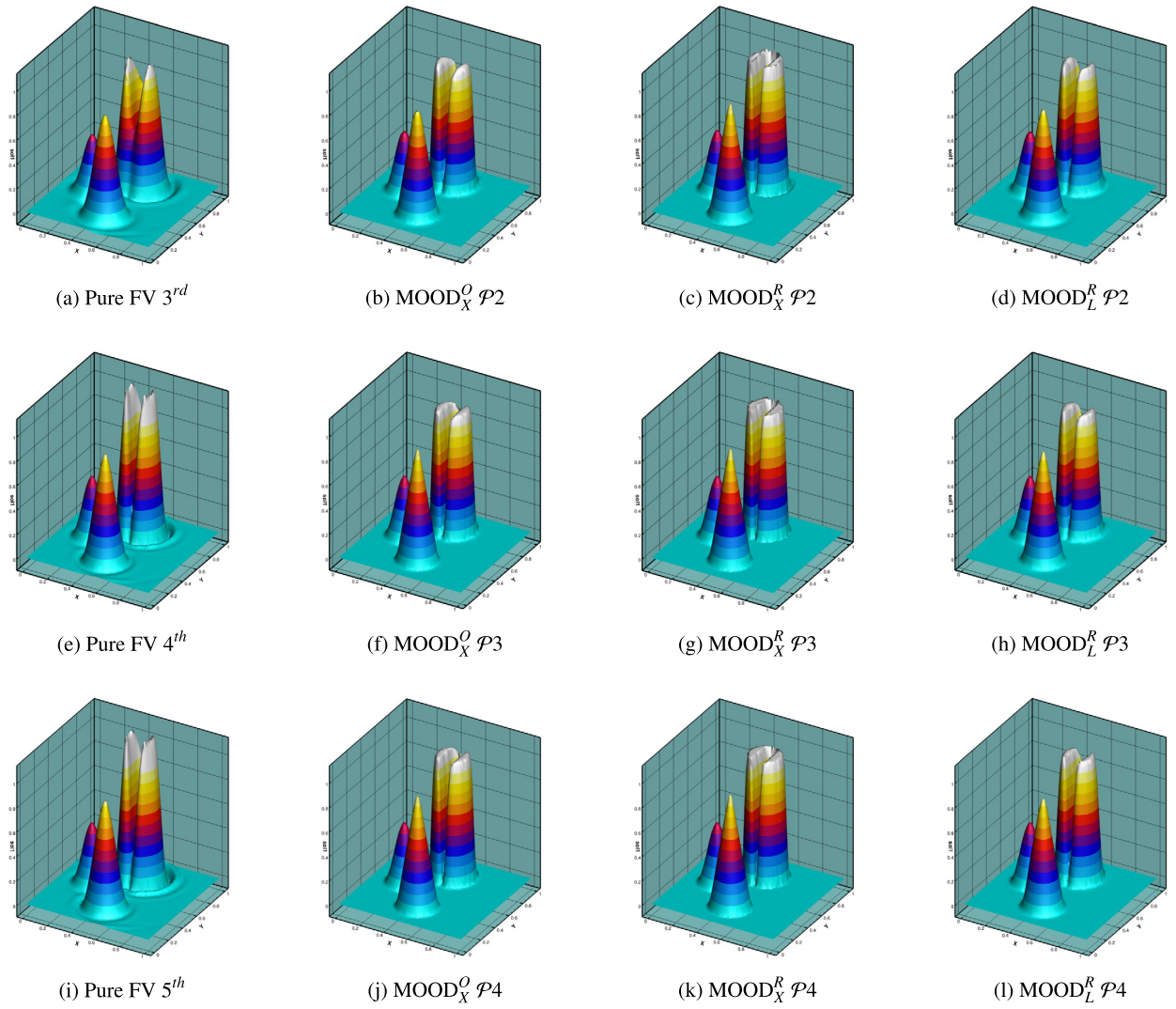

(a) Pure FV 3^{rd} (b) MOOD$_X^O$ $\mathcal{P}2$ (c) MOOD$_X^R$ $\mathcal{P}2$ (d) MOOD$_L^R$ $\mathcal{P}2$

(e) Pure FV 4^{th} (f) MOOD$_X^O$ $\mathcal{P}3$ (g) MOOD$_X^R$ $\mathcal{P}3$ (h) MOOD$_L^R$ $\mathcal{P}3$

(i) Pure FV 5^{th} (j) MOOD$_X^O$ $\mathcal{P}4$ (k) MOOD$_X^R$ $\mathcal{P}4$ (l) MOOD$_L^R$ $\mathcal{P}4$

Fig. 5. Computed results for the solid body rotation on hybrid mesh with 64 edges per side with 3^{rd}, 4^{th} and 5^{th} order polynomials.

eliminated with the more sensitive settings, i.e. with the MOOD$_X^O$ and MOOD$_L^R$ troubled cell indicators. The history of total percentage of troubled cells in the domain is reported in Fig. 6 and it is interesting to observe how the amount of troubled cells decreases with increasing accuracy orders, which is not causing an increased oscillatory behaviour. This counter-intuitive behaviour (one would have expected to have more troubled cells for higher orders), is due to the subcell capabilities of the DG scheme, as also reported in [66]. Hence, the final profile provided by the MOOD$_X^R$ indicator seems to be the less diffused, since the FV reconstruction is rarely activated. The effects of extended bounds on the troubled cells population can also be observed in Fig. 7, depicting the troubled cells at $t = 0.2s$ for four different configurations. When the bounds are only allowed to target a cell's direct side neighbours, an excess of cells is flagged as troubled, which causes overly diffused final shapes. On the other hand, the configuration with extended bounds marks as troubled only the cells at shape edges, and again coupled with a more conservative threshold value seems a good compromise to achieve good accuracy and limit the oscillations. The effect of allowing a troubled cell to change its condition within the RK stages of the same time steps is also represented (option referred as criterion1 in Fig. 2), and compared with the configurations where the cell condition is not allowed to change for a given time step (option referred as criterion2 in Fig. 2). The difference between these two settings seems negligible.

3.3. 2D Shu-Osher problem

The well established test case proposed by Shu-Osher [10] involves the interaction of a smooth entropy wave with a shock wave and is a popular benchmark for testing high-order accuracy methods. The computational domain is defined by $[-4.5, 4.5] \times [0, 1]$, with periodic boundary conditions applied along the y-axis, and supersonic inflow and outflow

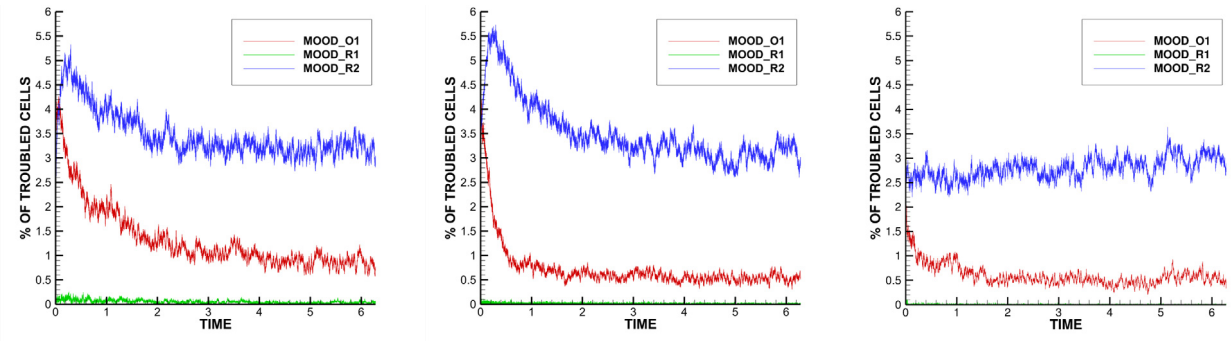

(a) DG($\mathcal{P}2$)-FV(CWENOZ3) (b) DG($\mathcal{P}3$)-FV(CWENOZ4) (c) DG($\mathcal{P}4$)-FV(CWENOZ5)

Fig. 6. Troubled cell history for different orders with 1=extended and 2=limited bounds.

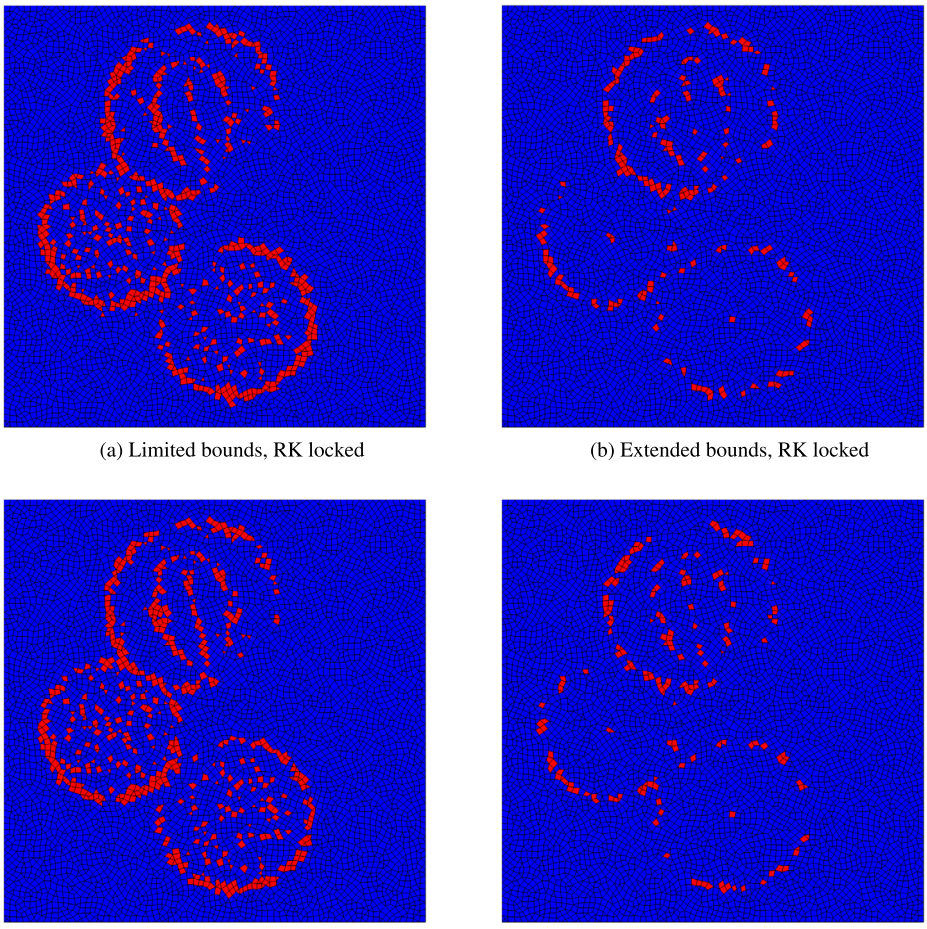

(a) Limited bounds, RK locked (b) Extended bounds, RK locked

(c) Limited bounds, RK unlocked (d) Extended bounds, RK unlocked

Fig. 7. Computed results for the solid body rotation on hybrid mesh with 64 edges per side with 3^{rd} order polynomial. With RK unlocked and locked we refer to criterion1 and criterion2 of Fig. 2 respectively.

applied on the left and right side of the domain respectively. The initial profile consists of a shock wave $(\rho, u, v, p) = (3.857143, 2.629369, 0, 10.333333)$ on the left when $x < -4$, and travelling over an entropy wave defined in the rest of the domain as $(\rho, u, v, p) = (1 + 0.2sin(5x), 0, 0, 1)$. A relatively coarse 2D triangular mesh is utilised with a resolution of each edge being $h = 0.070$ with approximately $13,000$ elements. The reference solution is computed with a solver of the one-dimensional Euler equations using $10,000$ grid points and employing a 5th order WENO scheme. The calculation is run until $t = 1.8$.

The results are presented in terms of density distribution plots in Fig. 8 for 3^{rd}, 4^{th} and 5^{th} order hybrid DG-FV(CWENOZ) scheme. The indicators tested are the MOOD^R with both extended and limited bounds and the SD with a value of 1.5 for the threshold parameter.

The results are in good agreement with the reference distribution and as expected the accuracy is improved when the discretisation order is increased. It has to be noted that for the lower order, the hybrid scheme shows a substantial improvement compared to the results provided by the pure FV scheme since a smaller portion of troubled cells is marked as troubled. However, when the polynomial order is increased, the pure FV scheme has a clear benefit in terms of agreement with reference, whereas this is not as noticeable for the hybrid scheme, especially when more sensitive indicators are used, as the solver resorts to the FV reconstruction more frequently. The troubled cells regions at final time are represented in Fig. 9, and is a good example of how the different troubled cell indicators work. The NAD detector of the MOOD type indicator checks whether the solution is monotonic, while the SD measures the total jump in the solution between the target and its neighbouring cells. This explains the more erratic behaviour of the former, while the SD consistently marks the cells crossed by the shock wave only. The adoption of limited bounds with MOOD^R indicator causes a larger portion of troubled cells aligned along the domain centreline and thus to a overly diffused profile correspondingly.

3.4. Double Mach reflection

The popular double Mach reflection test case of Woodward and Colella [74] is employed for assessing the accuracy and non-oscillatory properties of the hybrid scheme in presence of strong shocks. The problem consists of a shock wave moving diagonally with Mach number $M = 10$ and hitting a ramp inclined by $\alpha = 60°$, gradually generating secondary shock waves and triple points. The shock wave is initially located at $x = 1/6$, with reflecting boundary conditions applied at the bottom of the domain. At the top boundary the exact solution of an isolated moving oblique shock wave with $M = 10$ is prescribed. Ahead of the shock, the fluid is at rest with uniform density and pressure $\rho = 1.4$ and $p = 1.0$, and post shock conditions are assumed behind the shock front. At the left and right side of the domain, supersonic inflow and supersonic outflow boundary conditions are respectively applied.

For additional details regarding the setup of the problem the reader is referred to the original work of Woodward and Colella [74]. The computational domain is given by $[0, 4] \times [0, 1]$ and is discretised by an unstructured mesh of approximately $150,000$ triangular cells, that corresponds to an equivalent resolution of $h = 1/125$. A hybrid DG-$\mathcal{P}$3-FV(CWENOZ4) scheme is employed with MOOD^R, MOOD^O and SD troubled cell detectors, all adopted with the extended bounds option. The calculations are performed until time $t = 0.2$, using a CFL$= 0.5$ and $\lambda_1 = 10^7$. The results are presented in Fig. 10 for density contours and troubled cells.

Regardless of the troubled cell indicator being used, the hybrid scheme correctly captures the flow pattern with the incident, reflected, and Mach stem shock waves meeting in the first triple point. Again, the troubled cell plot highlights the different behaviours of MOOD and SD troubled cells indicators, with the latter being activated more consistently in correspondence of discontinuous features, while the former is activated in a wider range of situations, including steep gradients, pressure waves, and eventually by the grid topology itself. Looking closer at the triple point and wave interaction zone density contours in Fig. 11, some key differences can be observed on how the slipstream and the Mach stem are resolved. The only configuration that reproduces the onset of instabilities along the slipstream is with the less sensitive MOOD^R indicator, as both SD and MOOD^O leads to larger regions of troubled cells and thus to a more diffused solution correspondingly, failing to resolve the rolling of shear waves. Regarding the Mach stem, a curved profile was observed with all the troubled cell indicators. A curved Mach stem can be associated with the carbuncle sensitivity of the scheme, the misalignment of the shock wave with respect to the grid orientation itself, and other effects as documented in [75,76]. A workaround to limit the carbuncle effect is to perform the reconstruction using primitive variables instead of conserved variables. In Fig. 11, for comparison, the results are presented with reconstruction on conserved variables for MOOD type indicators, and on primitive variables for SD indicator, for which the carbuncle effect is less evident also considering the less propagated jet, and in agreement with results of Woodward and Colella [74].

3.5. Schardin's problem

The 2D test problem introduced by Schardin [77] is employed, where several flow structures are present that are ideal for assessing the non-oscillatory properties of the hybrid DG-FV framework. This problem involves a triangular wedge that is hit by a moving normal shock of Mach number $M_s = 1.34$. As the normal shock travels past the wedge, several flow structures emerge including contact waves, reflected shocks, vortices, and Mach stems. The computational domain has been defined to have the same dimensions as the experiment as described in [77], and we have applied reflective boundary conditions at the triangular wedge, top and bottom, while non-reflecting boundary conditions are applied at the right and left boundary, with the shock moving from left to right. A mixed-element unstructured mesh consisting of approximately $340,000$ cells consisting of quadrilaterals and triangles is used, with a refined region around the wedge corresponding to an average edge size of $h = 0.01$ mm as shown in Fig. 12. The initial conditions are given in Table (2), where $R = 287$ J/kg·K, the ratio of specific heats $\gamma = 1.4$, and the Euler equations are solved.

For this test problem we use the following methods, one pure FV variant employing the CWENOZ5 scheme, a hybrid DG-FV referred to as P3CWENOZ4 and a P4CWENOZ5 since it uses the same CWENOZ5 FV component. The relaxed MOOD

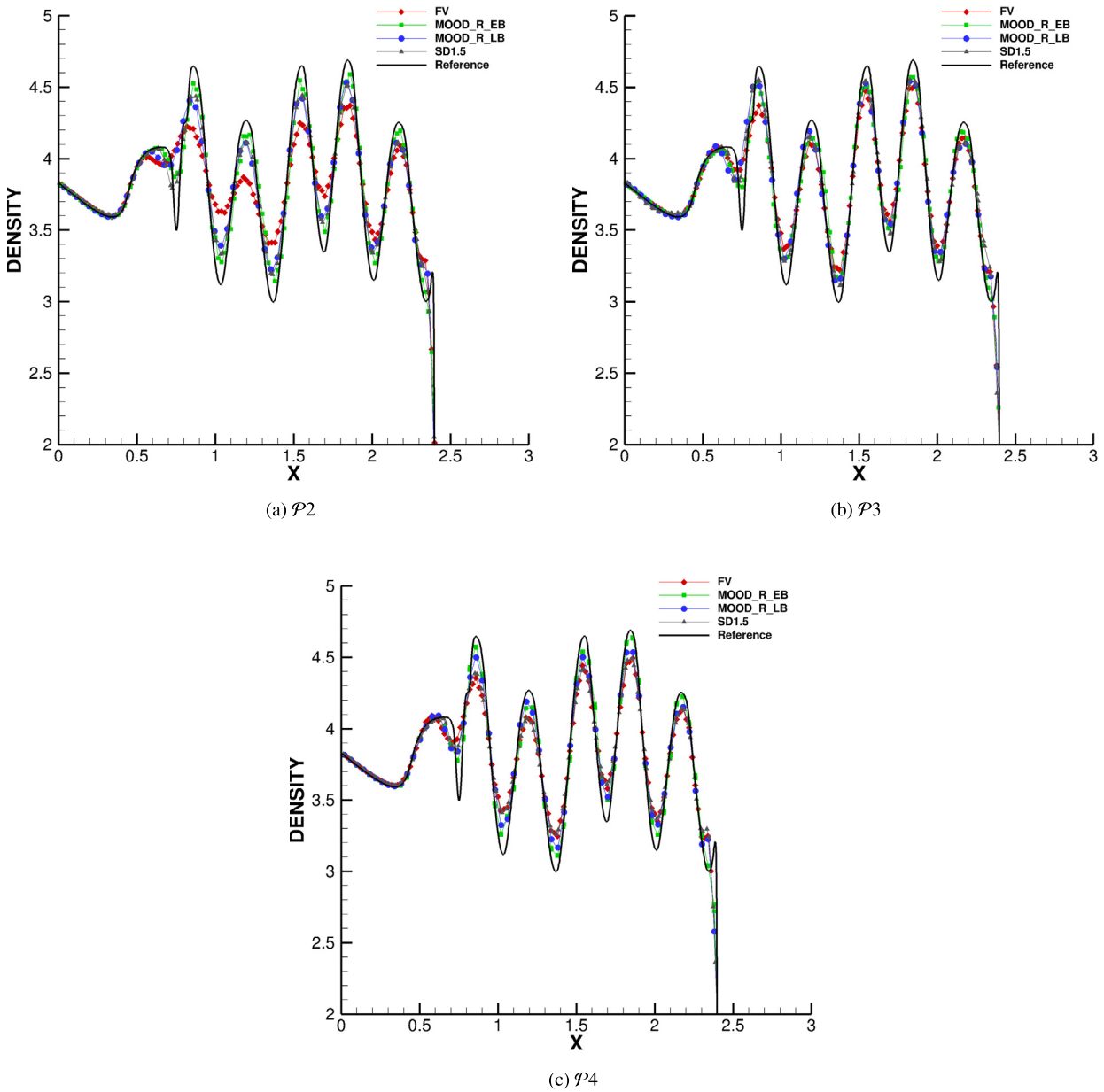

(a) $\mathcal{P}2$ (b) $\mathcal{P}3$

(c) $\mathcal{P}4$

Fig. 8. Density profiles for the Shu-Osher test case at time $t = 1.8$ obtained with hybrid DG-FV(CWENOZ) scheme with different troubled cells indicators and compared with FV and reference solutions.

Table 2
Initial Conditions for Schardin's test problem.

Parameter	Post-Shock	Pre-Shock
P (Pa)	195557.25	101325
T (K)	350.5	288.15
$\mathbf{u}$ (m/s)	(168.62,0,0)	(0,0,0)

type troubled cell indicator is used for the hybrid DG-FV variant. The solution is advanced in time with the 3rd-order SSP-Runge-Kutta with $CFL = 0.3$. The simulation is run for $t = 200$ ms from the time the normal shock contacts the wedge, which occurs at the start time of the simulation. From the obtained results with the hybrid DG-FV framework as shown in Fig. 13 it can be noticed that the obtained results agree well with the experiments of Chang and Chang [78], in terms of the flow structures that include the tip vortices, the bow shock, and the contact surfaces between the vortices and shock triple point. Comparing the solutions obtained from the three methods as shown in Fig. 14, it is evident that the hybrid DG-FV

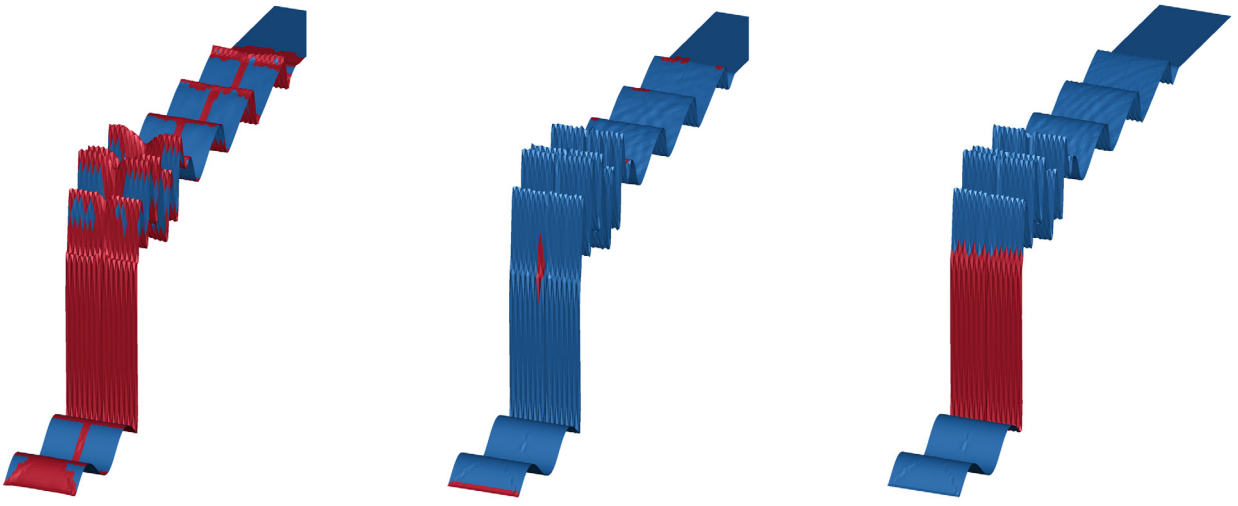

(a) $\mathcal{P}2/\text{MOOD}_L^R$ (b) $\mathcal{P}2/\text{MOOD}_X^R$ (c) $\mathcal{P}2/\text{SD1.5}$

Fig. 9. Profiles of Shu-Osher test case where troubled cells regions are highlighted in red, and resulting from MOOD and Shock Detector indicators with different threshold values.

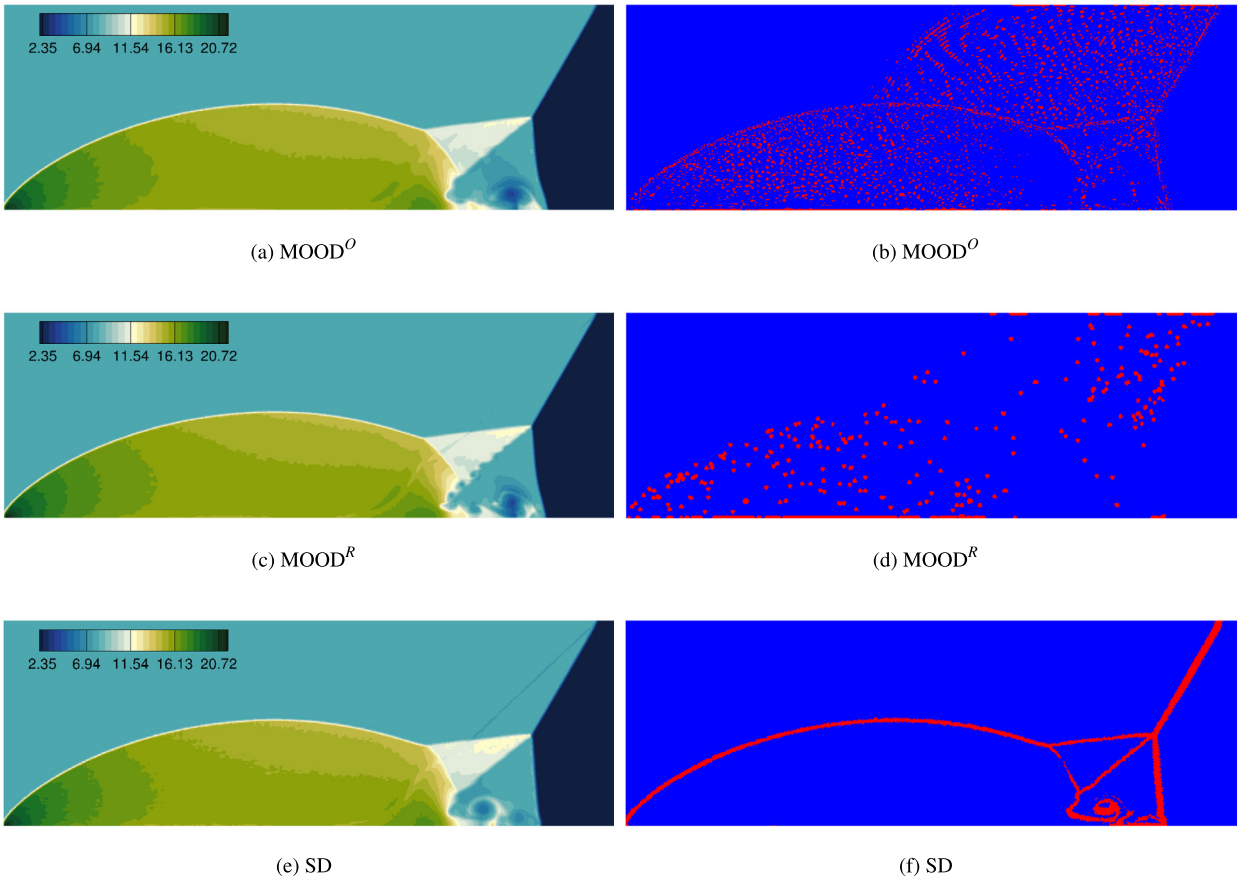

(a) MOOD^O (b) MOOD^O

(c) MOOD^R (d) MOOD^R

(e) SD (f) SD

Fig. 10. Density contours (*left*), and troubled cells (*right*), for the double Mach reflection test case at final time $t = 0.2$ with DG($\mathcal{P}3$)-FV(CWENOZ4) scheme and different troubled cell indicators.

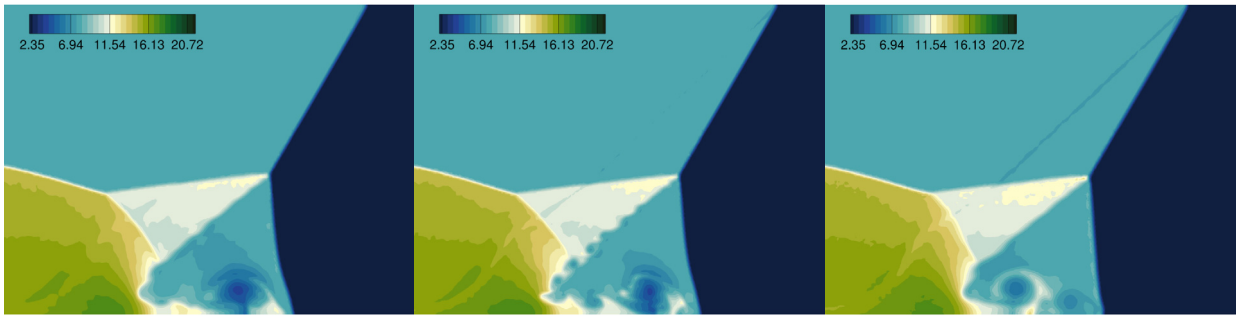

(a) DG-FV MOOD^O (b) DG-FV MOOD^R (c) DG-FV SD

Fig. 11. Zoom on the density contours of wave interaction regions. The onset of instabilities along the slipstream is more pronounced when a less sensitive troubled cell indicator, such the MOOD^R, is used. A curved Mach stem is noticed with all indicators, partially resolved when the reconstruction is performed using primitive variables instead of conserved variables, as presented for the SD indicator.

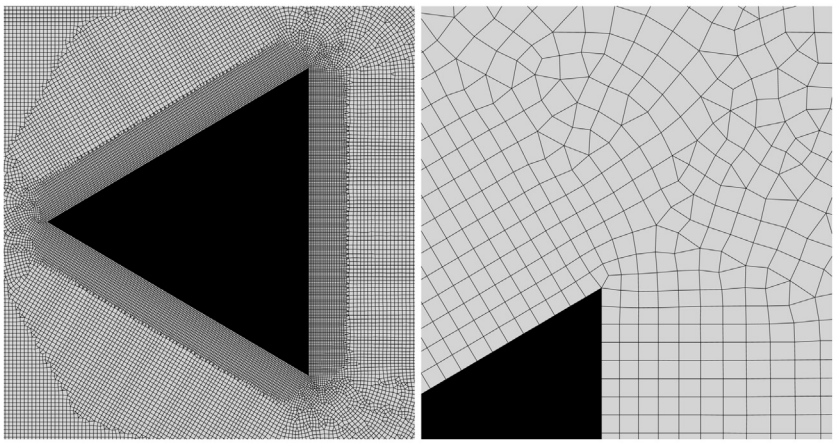

Fig. 12. Close-up of the mixed-element unstructured mesh used for the Schardin's test problem.

variants are able to resolve more structures and acoustic waves from the shock-vortexlet interactions, compared to the pure FV-CWENOZ5, but the CWENOZ component is of paramount importance to ensure the non-oscillatory properties without a severe reduction on the spatial accuracy at regions where it is activated.

Looking at the predicted Mach number distribution along the symmetry line of the triangular wedge of Fig. 15 at $t =$ 200 ms, it can be seen that the results between the three schemes agree well with each other, and the percentage of the troubled cells that resort to the FV-CWENOZ scheme are less than 0.4% and 0.2% throughout the duration of the simulation for the P3CWENOZ4 and P4CWENOZ5 schemes respectively.

3.6. Subsonic inviscid Taylor-Green vortex

The 3D inviscid subsonic Taylor-Green vortex test problem is used in order to understand the behaviour of the hybrid DG-FV framework in a setting where the flow is always "under-resolved" due to the lack of physical viscosity. This test problem reveals several characteristics (dissipation, dispersion etc.) of the numerical schemes which could be valuable when considering the extension of the schemes towards a large eddy simulation (LES). [41,52,79–89]. A coarse hexahedral mesh 64^3 is used to discretise the computational domain $\Omega = [0, 2\pi]^3$ with periodic boundaries and the initial condition which corresponds to a Mach number of $M \approx 0.08$ is given by the following profile of primitive variables:

$$u(\mathbf{x}, 0) = \sin(kx)\cos(ky)\cos(kz), \tag{47}$$

$$v(\mathbf{x}, 0) = -\cos(kx)\sin(ky)\cos(kz), \tag{48}$$

$$w(\mathbf{x}, 0) = 0, \tag{49}$$

$$\rho(\mathbf{x}, 0) = 1, \tag{50}$$

$$p(\mathbf{x}, 0) = 100 + \frac{\rho}{16}[\cos(2z) + 2] \cdot [\cos(2x) + \cos(2y)]. \tag{51}$$

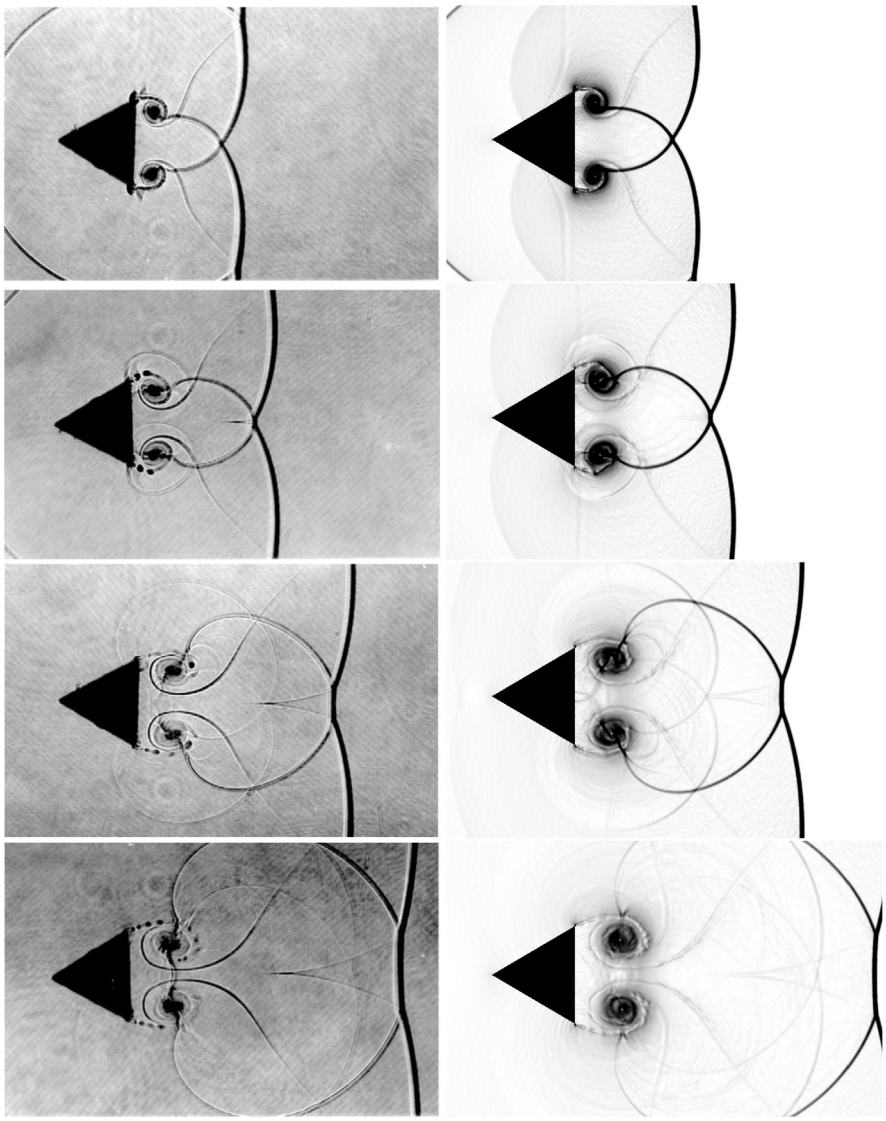

Fig. 13. Schlieren plot from experiment (left) [77] and density gradient (right) for DG(P4)-FV(CWENOZ5) for Schardin's problem.

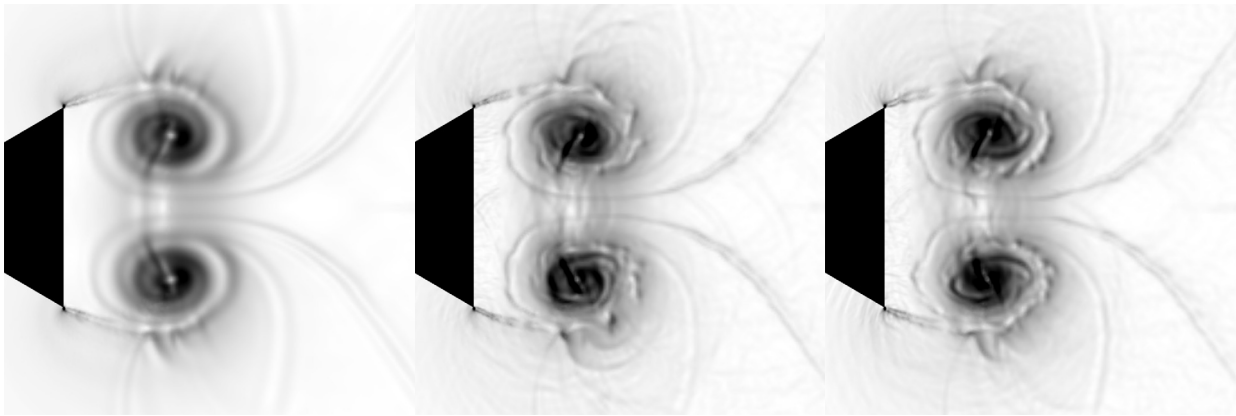

(a) FV(CWENOZ5) (b) DG(P3)-FV(CWENOZ4) (c) DG(P4)-FV(CWENOZ5)

Fig. 14. Density gradient at t=200 ms for Schardin's test problem obtained with the FV(CWENOZ5) DG(P3)-FV(CWENOZ4) and DG(P4)-FV(CWENOZ5) scheme.

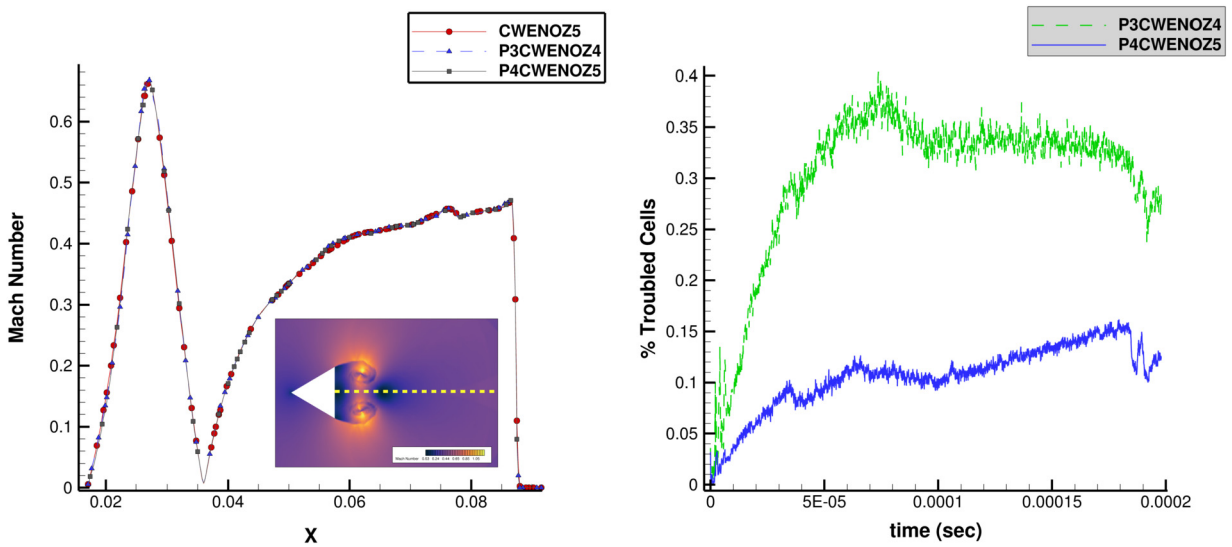

Fig. 15. Mach number distribution from the FV(CWENOZ4), the DG(P3)-FV(CWENOZ4) and the DG(P4)-FV(CWENOZ5) schemes (left) and troubled cells history for the DG(P3)-FV(CWENOZ4) scheme and DG(P4)-FV(CWENOZ5) schemes (right) for Schardin's test problem.

Four numerical schemes are used, two pure FV methods using a 3rd-order and 4th-order spatial CWENOZ schemes, and two hybrid DG-FV of 3rd-order and 4th-order of accuracy. For detecting the troubled cells the shock detector troubled cell indicator is used with the threshold value $C_k = 0.4$. The solution is advance in time with the 3rd-order SSP Runge-Kutta scheme with $CFL = 0.3$ until non dimensional time $t* = 14$, and the DNS results of Brachet et al. [90] are used for comparison. We can notice the typical behaviour of the transition of large symmetrical structures into smaller turbulent ones as shown in Fig. 16.

From the obtained results as shown in Fig. 17, it can be seen from the kinetic energy evolution with time that the hybrid DG-FV is outperforming the pure FV methods at the same grid resolution, as expected, while at the same time from the kinetic energy dissipation rate plot the DG-FV produces results closer to the DNS results. On a first read this is a desirable behaviour since the reduced numerical dissipation of the DG variant is producing results closer to the DNS results even at coarse grid resolution. However on a second read we notice that our implementation is not free from aliasing errors, something that is very well documented in the literature [91–95]. Another encouraging observation is that the simulation does not crash or diverge with the modal DG implementation currently employed, which does not use overintegration (also known as consistent integration), modal filtering, or split-form flux as reported by [93]. Examining the kinetic energy spectra at time $t = 10.0$, the hybrid DG-FV variant has a closer agreement with the theoretical Kolmogorov energy cascade for a wider-range of scales, which is indicative of the low-dissipation properties of the present framework, which can lead to significant improvements in the context of implicit or explicit LES simulations. The advantage of the very low dissipation of DG schemes is at the same time a bottleneck from the perspective that aliasing errors emerge, which can lead to stability issues, something that the high-order FV methods do not suffer from since they have significantly larger amount of dissipation. The situation is becoming more complicated by the fact that for a successful application of high-order methods for under-resolved turbulent flow simulations the “just right” amount of numerical dissipation is needed to ensure stability and physically meaningful results. In this front there are several elegant techniques that have been developed towards this goal such as overintegration [91], explicit filtering of high-order modes that are responsible for aliasing errors [94,96], and split-form flux approximation [91]. All of these techniques still have room for improvements such as the overintegration, which is computationally expensive, without a guarantee that aliasing errors will not appear at severe under-resolved situations, or the explicit filtering for the higher-order modes that is quite ad-hoc in nature and striking the perfect balance between accuracy and stability is far from obvious. We plan to further investigate the suitability of several mechanisms in the future for reducing the aliasing errors of the present modal-DG component of our hybrid DG-FV framework.

3.7. Supersonic inviscid Taylor-Green vortex

An interesting variation of the Taylor-Green vortex flow problem involves the supersonic variant which is mostly targeted towards assessing the non-oscillatory properties of the developed framework. It was recently introduced by Lusher and Sandham [97] and is better suited for numerical methods intended for compressible flow problems. The computational domain and the velocity field remain the same as the subsonic variant previously described and the parameters that change are the pressure field:

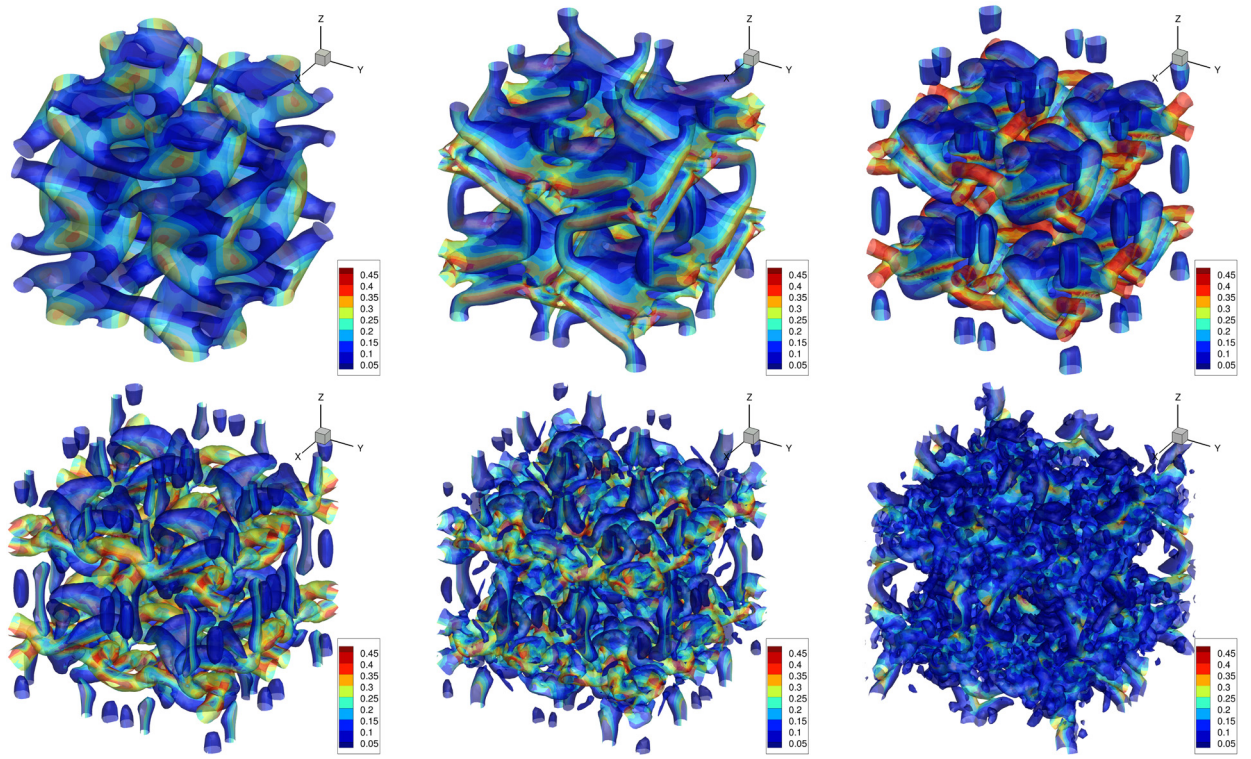

Fig. 16. Solution of the Taylor-Green vortex flow computed with the DG(P3)-FV(CWENOZ4) on a hexahedral mesh of 64^3. The isosurfaces of the Q-criterion Q=2.5, coloured by the kinetic energy are plotted at times $t = 2, 4, 5, 6, 8$ and 10 from top left to bottom right respectively.

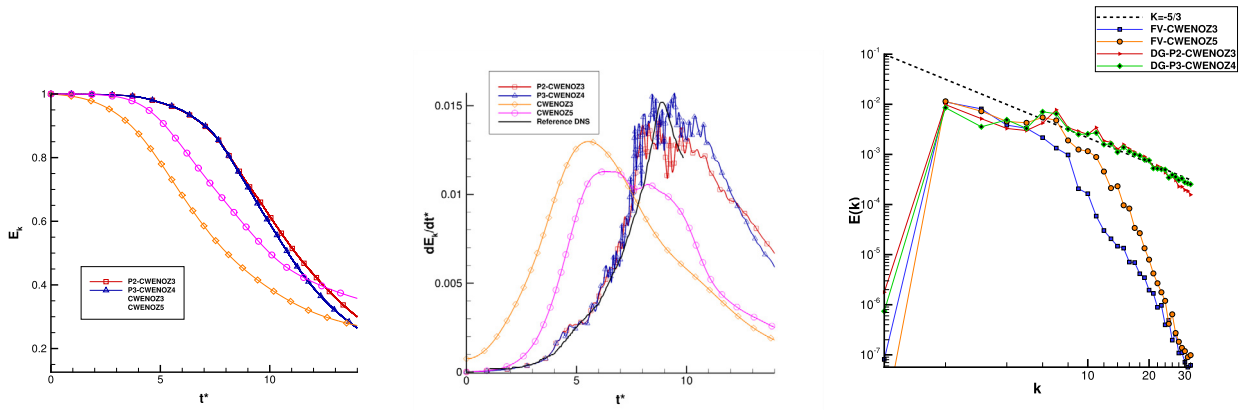

Fig. 17. Kinetic energy evolution with time (left), kinetic energy dissipation rate (middle) and kinetic energy spectra at $t = 10.0$ for the subsonic inviscid Taylor-Green Vortex obtained with various schemes on a 64^3 hexahedral mesh, and comparison with the DNS results of Brachet et al. [90]. DG-FV is superior at the same resolution for kinetic energy spectra where a closer agreement with the Kolmogorov's slope is obtained, but the aliasing errors present at the kinetic energy dissipation rate point to improvements required such as split-form flux, overintergration or filtering.

$$p(x, y, z, 0) = \frac{1}{\gamma M_{ref}^2} + \frac{1}{16}[\cos(2z) + 2] \cdot [\cos(2x) + \cos(2y)], \tag{52}$$

and the density which is computed from the equation of state.

We only examine the variant with a Mach number $M_{ref} = 1.25$ and the simulations were carried out on a hexahedral mesh of 64^3 with several orders of the DG-FV framework, as well as on a hexahedral mesh of 128^3 with a fourth-order DG-FV scheme. All of the methods were augmented by the shock-detector type indicator with a threshold value $C_k = 0.2$. A CFL number of 0.3 is used for the explicit Runge-Kutta 3rd-order scheme, up to $t = 20$ for obtaining the required statistics. The results of Lusher and Sandham [97] are used for comparison against the computed solutions.

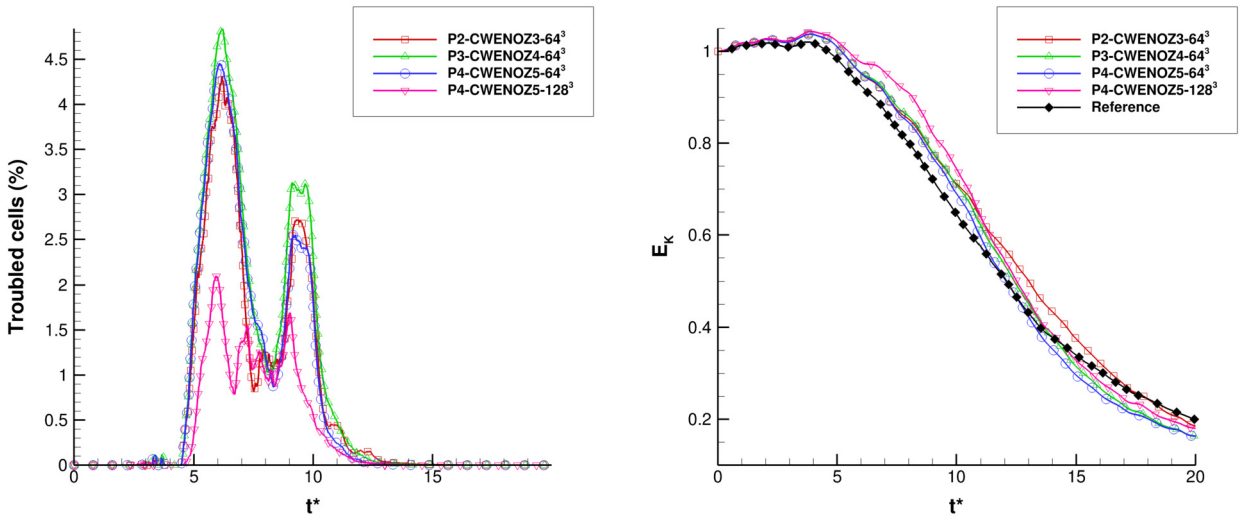

Fig. 18. Evolution of the percentage of the troubled cells (left) and kinetic energy (right) for the supersonic Taylor-Green vortex flow computed with the several schemes of the present framework and comparison with the reference results of Lusher and Sandham [97] obtained at a resolution of 512^3 with a 5th-order accurate WENO scheme.

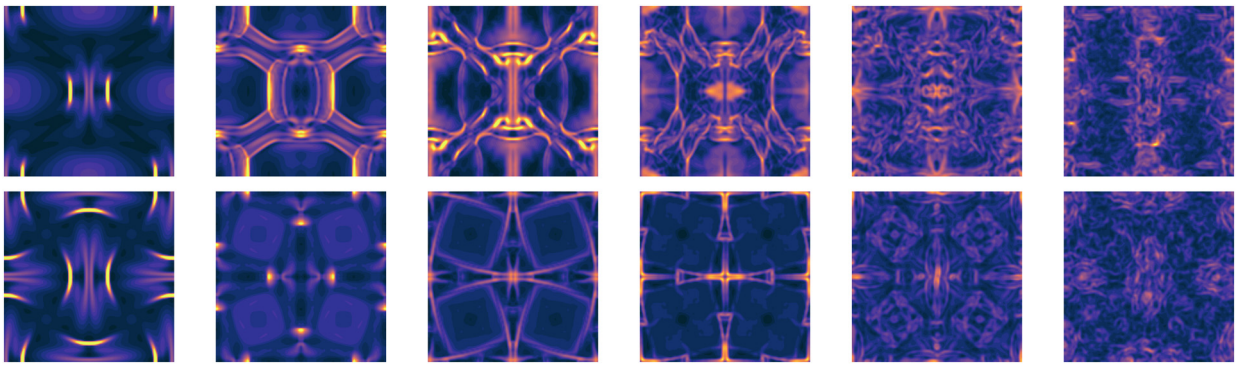

Fig. 19. Contour plots of the density gradient for the supersonic Taylor-Green vortex flow computed with the DG(P4)-FV(CWENOZ5) on a hexahedral mesh of 128^3 at the $Y = \pi$ (top) and $Z = \pi$ (bottom). The contour plots at times $t = 2, 4, 6, 8, 10$ and 12 from left to right.

From the obtained results as shown in Fig. 18 it can be noticed that the percentage of the troubled cells suddenly increases between $t = 5 - 12$ for all the schemes, and as the resolution of the mesh is increased the percentage of troubled cells is also reduced. Examining the kinetic energy evolution as a function of time it can be seen that a close agreement is obtained with the reference results of Lusher and Sandham [97] at a resolution of 512^3 with a 5th-order accurate WENO scheme. It has to be stressed however that our setup is inviscid and therefore a converged solution at the absence of viscosity can not be obtained. Nonetheless, this problem is ideal for assessing the non-oscillatory properties of the framework where it is robust enough to not be put at risk of diverging from the strong-gradients present, or the aliasing errors identified previously. Additionally, we plot the density gradient magnitude at the middle of the Z-axis (XY plane) and Y-axis (XZ plane) on the finest hexahedral mesh of 128^3 obtained with DG(P4)-FV(CWENOZ5) in Fig. 19, where the similar patterns as Lusher and Sandham [97] are noticed up to $t* = 10$, since due to absence of viscosity the setup is significantly different at late times.

Finally, in Fig. 20 we have also plotted the troubled cells in the domain for the DG(P4)-FV(CWENOZ5) on the finest hexahedral mesh at different instants where it can be noticed that the number of cells reduce at later times, and these are the regions where the high-order CWENOZ5 component is activated.

3.8. Sonic boom prediction of LM1021

The final test problem involves the prediction of the near-field pressure signature of the supersonic Lockheed Martin 1021-01 model from the first sonic boom prediction workshop [98]. The key aim of this workshop was to utilise CFD methods to better understand the acoustic footprint predicted from different models. This in turn could lead to solutions for minimising the sonic boom from supersonic aircraft and therefore making their use more environmentally friendly. A perspective of the model can be seen in Fig. 21, and the primary goal for employing this test is to assess the robustness and

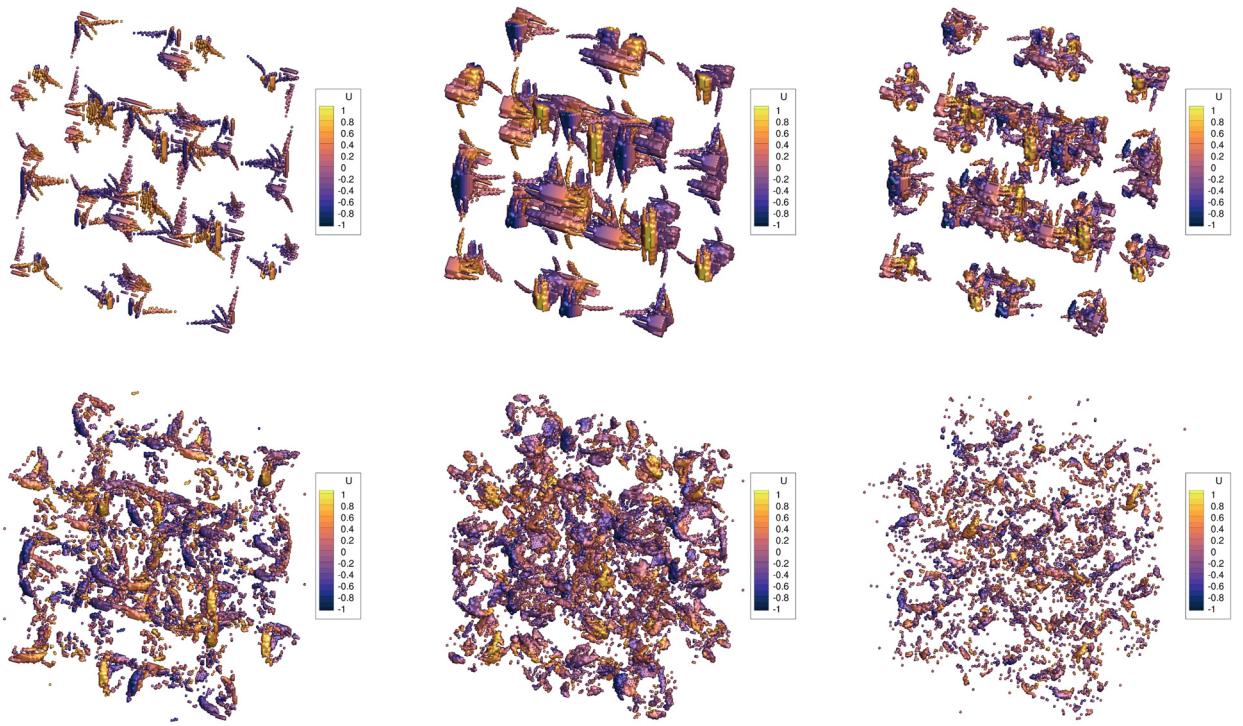

Fig. 20. Troubled cells coloured by the x-velocity for the supersonic Taylor-Green vortex flow computed with the DG(P4)-FV(CWENOZ5) on a hexahedral mesh of 128^3 at times $t = 5, 6, 7, 8, 9$ and 10 from top left to bottom right respectively.

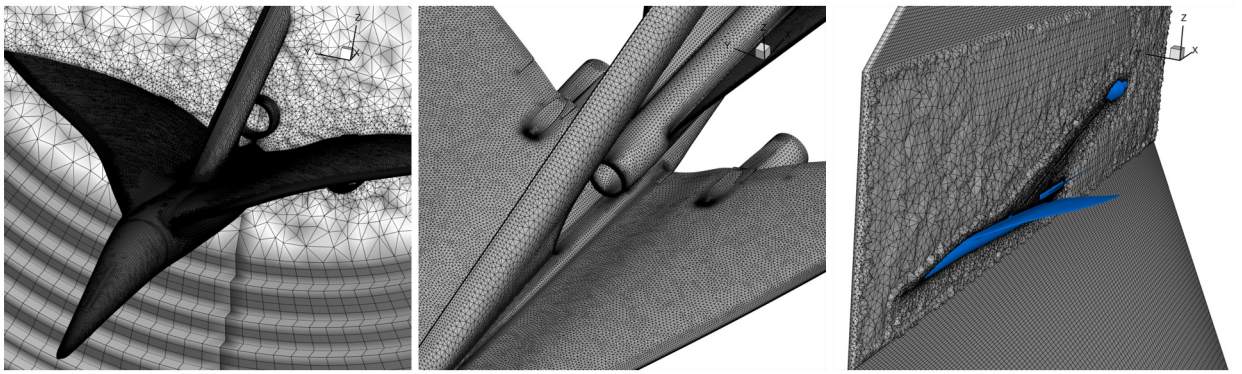

Fig. 21. Sonic boom prediction mesh.

accuracy of the hybrid DG-FV framework on an aeronautical configuration that includes flow regions of strong gradients, while utilising the coarsest hybrid unstructured mesh provided in the first sonic boom prediction workshop [98] that consist of approximately 5,3 million cells. The mesh used is significantly coarser from most of the meshes used in the workshop where the mesh sizes ranged from 13-57 million for the Euler equations simulations. The flow conditions include a free stream Mach number $M_\infty = 1.6$ and angle of attack of 2.3 degrees, and due to the fact that the provided grid is oriented at this incidence we run the simulation at 0 degrees angle of attack. We solve the 3D Euler equations using two schemes, the high-order FV CWENOZ3 and the hybrid DG-FV (P2CWENOZ3) with the shock detector indicator with the threshold value $C_k = 0.2$ and a local-time stepping is used with a $CFL = 0.3$ for accelerating the simulation to reach a steady state. The simulation is deemed converged when the integrated forces do not change more than ± 0.001. The mesh consists of tetrahedral cells close to the LM1021 model, and away from the model hexahedral elements are used, with the interface between them being accommodated by pyramidal elements as shown in Fig. 21. Supersonic inflow and outflow boundary conditions are applied at the entire computational domain, except at surface of the LM1021 model where wall boundaries are defined, and the symmetry boundary conditions at the symmetry plane since half of the model is used.

The parameter that we are focusing on in terms of the results is the pressure signature $\Delta P/P_\infty$ similarly to the workshop [98]. From the obtained results as shown in Fig. 22, it can be noticed that the pressure signature predictions from both

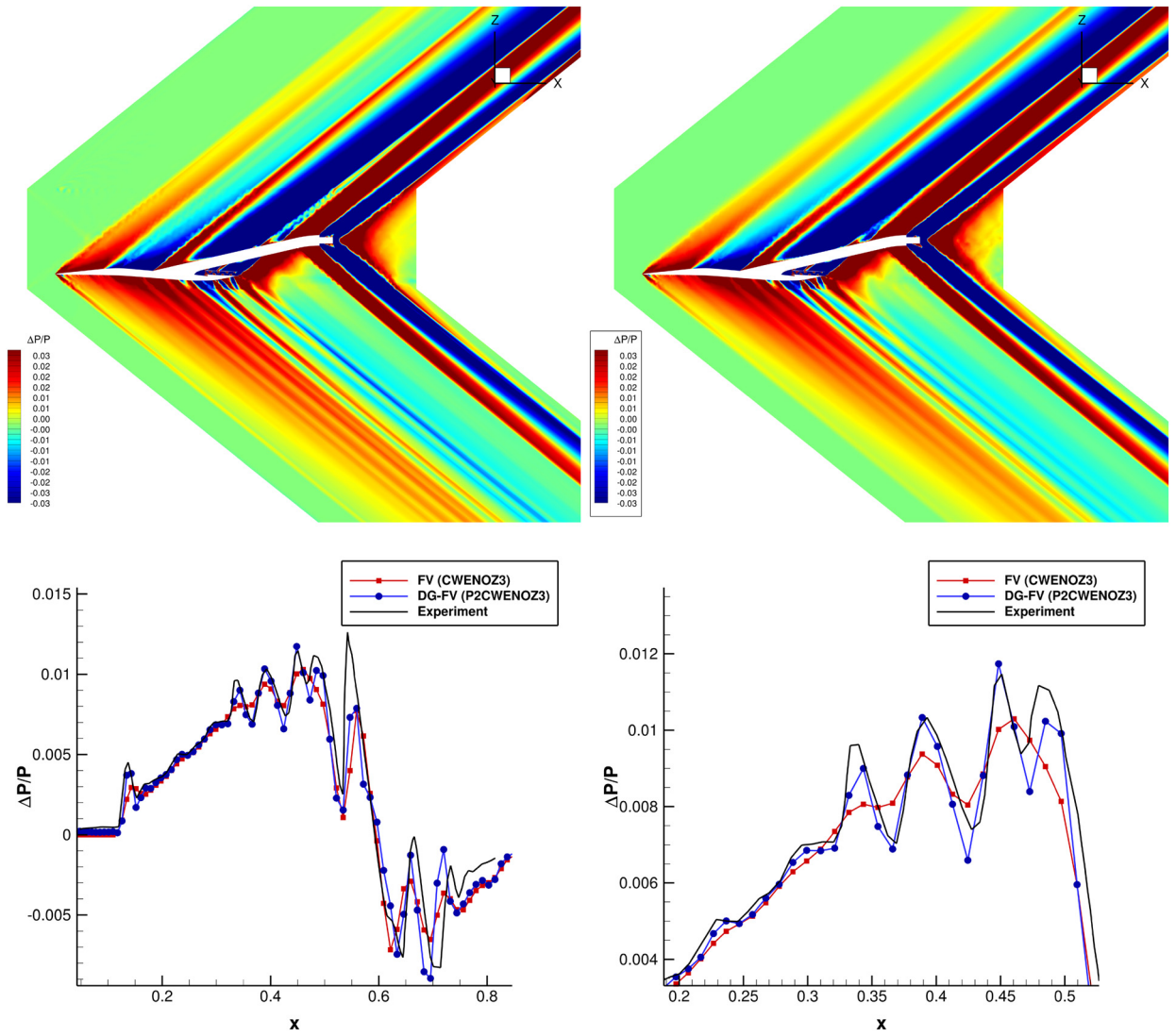

Fig. 22. Contour plots of pressure signature (top) for the hybrid DG-FV (P2CWENOZ3) scheme (left) and the FV (CWENOZ3) scheme, and the pressure signature (bottom) at 31.8 inches below the model obtained with both schemes and comparison with the experimental results from the sonic boom prediction workshop [98]. It can be noticed that the hybrid DG-FV provides the closest agreement with the experimental results.

variants FV and hybrid DG-FV are similar at least in the contour plots at the centreline ($\phi = 0$) of the domain. When extracting the same signature at the centreline ($\phi = 0$) of the domain but at 31.8 inches away from the model and compare the results against the experimental results at the same location some distinct differences between the schemes can be noticed. The hybrid DG-FV variant is able to obtain a closer agreement with the experimental results primarily due the largest peaks obtained compared to the pure FV variant, and it is remarkable that his result is achieved at such coarse grid resolution where only 45 cells are used for the entire model at 31.8 inches away from the model.

Finally we can notice the pressure coefficient distribution on the surface of the LM1021 obtained with the hybrid DG-FV scheme, where the location of the shocks is evident and in agreement with the computational and experimental results from the sonic boom prediction workshop [98]. Additionally we plot the cells that are deemed as troubled and are solved by the FV-CWENOZ3 method (Fig. 23).

4. Conclusions

This paper details a family of high-order, non-oscillatory, hybrid DG-FV schemes for mixed-element unstructured meshes up to 5th-order spatial accuracy. The schemes are able to achieve the accuracy characteristic of DG schemes in smooth flow regions, maintaining robustness and avoiding unphysical oscillations in the presence of discontinuous flow features. This is accomplished without a significant increase in computational effort by switching to a high-order FV(CWENOZ) method when troubled cells are detected. A variety of configurations for the *a priori* troubled cell detection were tested, including but not

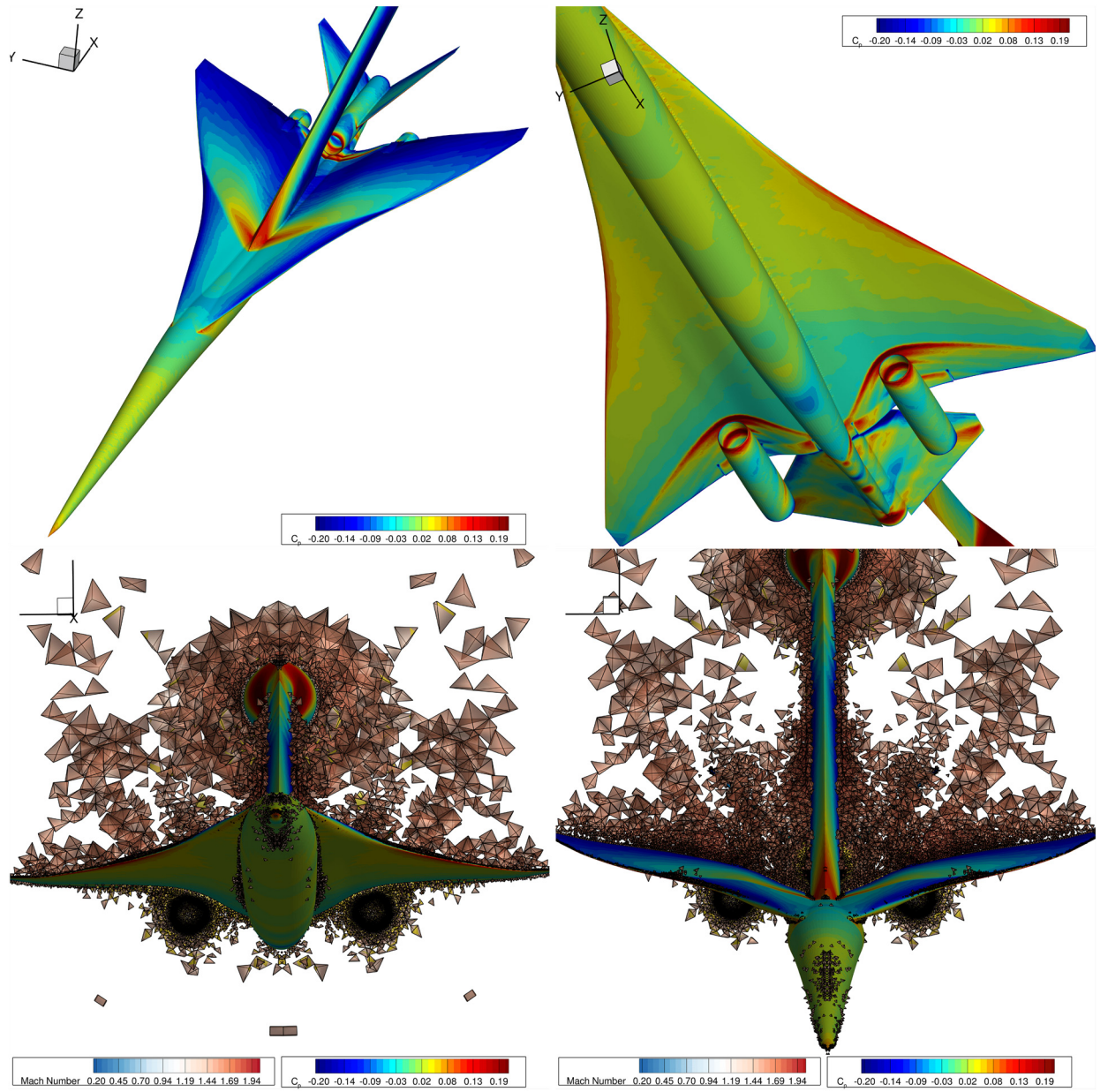

Fig. 23. Contour plots of the pressure coefficient on the surface of the LM1021, and troubled cells coloured by the Mach number obtained with the hybrid DG-FV (P2CWENOZ3) scheme.

limited to MOOD^O, MOOD^R and shock detector. Additionally we investigated the influence of the bounds definition, and frequency of checking for troubled cells. It was found that reducing the number of troubled cells detected, as expected, provides higher accuracy and better resolution of flow features. Using extended bounds MOOD with a more restrictive threshold provided the best balance of accuracy and lack of oscillations for simple test cases, but a relaxed threshold was required to resolve the shear vortices in the double Mach reflection problem. However, the shock detector was found to be more consistent in marking the zones with physical discontinuities only. Application to the Taylor-Green vortex demonstrates that the hybrid DG-FV scheme is able to better match the dissipation rate of the reference DNS values, as well as the theoretical Kolmogorov kinetic energy spectra. However, the solution is still affected by instabilities in the high-energy modes from the DG component, for which we will investigate several mechanisms available to reduce them in the future, since the choices are far from obvious or unique. The present hybrid DG-FV provided significant benefits in resolving the pressure signature of a model supersonic airliner using a coarse hybrid unstructured mesh where several shock waves are present. The hybridisation of high-order DG and high-order FV methods has demonstrated, that it has the potential to improve further their robustness and accuracy. The very fine tuning of the criteria for switching from DG to FV is not a necessity since a high-

order CWENOZ variant of same order of accuracy is used, on the other hand when there is a mismatch in spatial order of accuracy (e.g. when using a 2nd-order FV method) fine tuning is mandatory. All the methods have been implemented and have been made available to the research community in the open-source `UCNS3D` CFD solver to accelerating the adoption of the methods. Other future work will include the search for an effective, parameter-free troubled cell indicator, subcell limiting that handles efficiently poor quality elements, and extension to viscous flows and multiphysics applications.

CRediT authorship contribution statement

Vadim Maltsev: Conceptualization, Formal analysis, Methodology, Software, Visualization, Writing – original draft, Writing – review & editing. **Dean Yuan:** Conceptualization, Formal analysis, Methodology, Software, Visualization, Writing – original draft, Writing – review & editing. **Karl W. Jenkins:** Supervision, Writing – review & editing. **Martin Skote:** Supervision, Writing – review & editing. **Panagiotis Tsoutsanis:** Conceptualization, Formal analysis, Funding acquisition, Methodology, Resources, Software, Supervision, Visualization, Writing – original draft, Writing – review & editing.

Declaration of competing interest

The authors declare that they have no known competing financial interests or personal relationships that could have appeared to influence the work reported in this paper.

Data availability

The datasets of the test problems in this article are available at the Cranfield Online Research Data repository 10.17862/cranfield.rd.21436389.

Acknowledgements

The authors would like to thank the reviewers for their constructive comments and feedback that greatly improved this manuscript. The authors acknowledge the computing time on ARCHER2 through UK Turbulence Consortium [EPSRC grant number EP/L000261/1 and EP/R029326/1]. V.M, M.S and P.T acknowledge the support from EPSRC (Grant No. 2497012), Innovate UK (Grant No. 263261), and Airbus Operations limited. P.T also acknowledges the support provided by the EPSRC grant for “Adaptively Tuned High-Order Unstructured Finite-Volume Methods for Turbulent Flows” [EPSRC grant number EP/W037092/1].

Appendix A. Bounds definition

The troubled cell indicators were original designed following the principle of TVB type limiters, hence using information from the neighbouring cells to determine if certain condition, with respect to the target cell, were violated and then enabling a limiting function in order to cancel out possible numerical artifacts. When applied to unstructured meshes, these limiters can experience different behaviours based on the number of neighbouring cell layers, which in turn depends on arguments like mesh quality, reconstruction robustness and computational budget. An investigation on stencil selection algorithms was conducted in [55], and in [30] the impact of different bounds definitions on the accuracy of MUSCL type scheme demonstrated that using a stencil composed by direct side neighbouring cells only, is often the reason for reduced order of accuracy. This is due to the activation of the limiter in smooth flow regions, which can occur because although the unlimited reconstruction can provide a non-oscillatory solution, the bounds imposed by the direct side neighbours (coloured in yellow in Fig. A.24) provides an extremely narrow range of admissible solutions. In addition, things can worsen in presence of bad quality cell elements, as the limiter itself can be activated by the condition number of the resulting reconstruction system. In order to achieve higher orders of accuracy, the bounds should be extended to the entire stencil (composed by the set of grey, yellow and red cells in Fig. A.24). The numerical results in [30] demonstrate that this redefinition of the bounds allows to reach up to 4^{th} order of convergence with a MUSCL scheme with the Michalak and Ollivier-Gooch limiter [99].

This raises the question of how the redefinition of the bounds can impact the detection of the troubled cells in the case of an unlimited DG solution. Theoretically, and as we will be able to verify in numerical experiments, the extension of the bounds to the entire stencil has a beneficial impact on the detection of the troubled cells, especially in smooth flow regions. Hence, the troubled cell indicators discussed in Section 2.5 are tested with both limited and extended bounds definition, where the minimum and maximum values to be used in the indicators, are defined respectively by:

$$U_i^{minL} = \min(U_n : n = 1, ..., N) \text{ and } U_i^{maxL} = \max(U_n : n = 1, ..., N), \tag{A.1}$$

$$U_i^{minE} = \min(U_m : m = 1, ..., M) \text{ and } U_i^{maxE} = \max(U_m : m = 1, ..., M). \tag{A.2}$$

In the above, the index n ranges from the target element to the last neighbouring element N for the limited bounds stencil, labelled with the superscript L, while the index m ranges from the target cell to the last neighbouring element M of the entire stencil for the extended bounds case, labelled with superscript E.

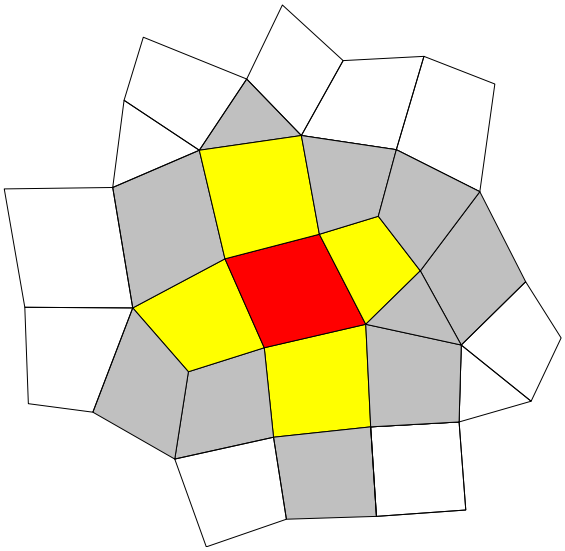

Fig. A.24. Example of stencil for 4^{th} order reconstruction on unstructured mesh. The limited bounds, as defined in text, refers to the stencil formed by the target cell, coloured in red, and its direct side neighbours, coloured in yellow. The extended bounds are defined by the entire set of red, yellow and grey cells of the total stencil.

Appendix B. Linear advection of smooth profile

The performance of pure FV, DG, and hybrid FV/DG schemes is first tested and compared for the 2D linear advection of a smooth function $U(x, y, 0) = \sin(2\pi x) \cdot \sin(2\pi y)$ on a computational domain defined by $[0, 10] \times [0, 10]$ with periodic boundary conditions applied on all sides. Three types of meshes are used, including a uniform quadrilateral, a triangular, and a hybrid unstructured mesh composed of mixed elements, as shown in Fig. 3, with four different resolutions corresponding to 16, 32, 64, and 128 edges per side for $\mathcal{P}2$ and $\mathcal{P}3$; and 8, 16, 32, and 64 for $\mathcal{P}4$. The computations are run for one period and the e_{L^2} error is computed at the final time according to Eq. (39). The computations are performed using CFL$= 0.5$ and a value $\lambda_1 = 10^7$ for the central stencil for the CWENOZ reconstruction in the troubled cells.

The purpose of this test is to assess the accuracy of the solution obtained with the FV scheme with CWENOZ reconstruction and the DG scheme, which then are used as a benchmark for the performance of the hybrid DG-FV scheme.

The results are presented in Table (B.3) and they have to be carefully interpreted. Ideally, for smooth problems, the troubled indicator should not detect any troubled cells and the reconstruction should not be activated at all. However, it is typical of the majority of the troubled indicators to detect erroneously invalid cells around smooth extrema. Indeed, this is the case with both the indicators investigated in this test case, i.e. the PAD/NAD detectors defined in the MOOD paradigm and here simply labelled as the MOOD detector as in Eq. (36), and the shock detector defined as in Eq. (35), where the checking criteria are applied to the scalar variable. Assuming that both the pure FV and DG schemes are able to achieve the theoretical order of convergence, it is expected that the hybrid scheme will retain, at least, the same order of convergence. The pure FV and DG schemes are close to the theoretical order of convergence, although a smaller time step size would be beneficial to get closer to target order with the FV scheme, whereas for the DG scheme, the obtained convergence is impacted by round-off errors. On the other hand, it is practically difficult to determine the order of convergence of the hybrid scheme in a consistent way. One way to test the effectiveness of the FV and DG blending is to render artificially all the cells as troubled, and therefore enable the CWENOZ reconstruction for the higher DOFs everywhere in the domain. The results for this test are presented in Table (B.4) for the quadrilateral mesh, and demonstrate that the procedure is able to preserve the expected order of convergence even with all the cells considered troubled, although the resulting accuracy is generally more comparable to the pure FV scheme.

For more realistic situations, where troubled cells are actually determined by the activation of the detectors, a mesh refinement will inherently bring a decrease in the percentage of troubled cells in the domain (see Table (B.3)), undermining the consistency of the convergence study. In other words, since for coarser meshes the accuracy is heavily impacted by the higher number of cells where the reconstruction is enabled, it is difficult to compare it with refined meshes where the majority of the cells is using a pure DG scheme. Although this explains the higher rate of convergence observed for the hybrid DG-FV in Table (B.3) with both detectors, it is nevertheless interesting to observe how the decrease in percentage of troubled cell due to mesh refinement, affects the accuracy and the computational time with different detectors. Whereas the amount of troubled cells detected with the MOOD indicator is generally very small and located near the position of the peaks of the advected function, the shock detector, which is not really intended for this kind of scalar problems, clearly erroneously detects a majority of troubled cells. As expected, a larger population of troubled cells causes an accuracy degradation and an increase in computational time. In order to quantify the latter, we express it through a coefficient,

Table B.3
Values for e_{L^2} error and convergence rates for pure FV and DG framework, and hybrid DG-FV with the MOOD^O and SD troubled cell indicators, for smooth profile advection test. For the hybrid schemes the average percentage of troubled cells are averaged on the total number of time steps and the additional costs for the reconstruction in the troubled cells is quantified though the CPU coefficient normalised with the pure DG computational time on the same mesh and polynomial order.

Order/Number of Edges	FV		DG		DG/MOOD^O				DG/SD			
Quadrilateral Mesh	e_{L^2}	$\mathcal{O}_{L^2}$	e_{L^2}	$\mathcal{O}_{L^2}$	e_{L^2}	$\mathcal{O}_{L^2}$	% troub. cells	CPU	e_{L^2}	$\mathcal{O}_{L^2}$	% troub. cells	CPU
$\mathcal{P}2/16$	9.14E-02	-	8.80E-05	-	1.92E-03	-	4.53	1.06	2.64E-02	-	27.9	1.25
$\mathcal{P}2/32$	1.30E-02	2.81	3.05E-06	4.85	7.77E-05	4.63	1.09	1.05	2.35E-03	3.49	13.7	1.06
$\mathcal{P}2/64$	1.66E-03	2.97	1.23E-07	4.63	2.99E-06	4.70	0.27	1.08	2.48E-04	3.24	6.73	1.10
$\mathcal{P}2/128$	2.08E-04	2.99	7.33E-09	4.07	1.08E-07	4.79	0.07	1.04	2.82E-05	3.14	3.24	1.05
$\mathcal{P}3/16$	7.28E-03	-	2.83E-07	-	7.37E-04	-	4.87	1.05	6.82E-03	-	97.8	1.70
$\mathcal{P}3/32$	3.70E-04	4.30	5.36E-09	5.72	3.88E-05	4.25	1.21	1.01	3.10E-04	4.46	65.7	1.67
$\mathcal{P}3/64$	3.45E-05	3.43	2.87E-10	4.22	1.47E-06	4.72	0.30	1.02	2.13E-05	3.86	36.3	1.51
$\mathcal{P}3/128$	2.77E-06	3.64	2.27E-11	3.66	4.90E-08	4.91	0.07	1.01	9.85E-07	4.44	18.2	1.08
$\mathcal{P}4/8$	1.66E-01	-	7.80E-07	-	1.60E-02	-	20.1	1.09	2.57E-01	-	100	1.58
$\mathcal{P}4/16$	7.61E-03	4.45	8.67E-09	6.49	2.03E-04	6.29	4.70	1.05	1.50E-02	4.10	100	1.73
$\mathcal{P}4/32$	2.75E-04	4.79	2.32E-10	5.22	1.95E-06	6.70	1.17	1.03	5.20E-04	4.85	99.3	1.71
$\mathcal{P}4/64$	1.17E-05	4.55	1.04E-11	4.48	1.88E-08	6.68	0.30	1.02	2.06E-05	4.66	80.6	1.64
Triangular Mesh	e_{L^2}	$\mathcal{O}_{L^2}$	e_{L^2}	$\mathcal{O}_{L^2}$	e_{L^2}	$\mathcal{O}_{L^2}$	% troub. cells	CPU	e_{L^2}	$\mathcal{O}_{L^2}$	% troub. cells	CPU
$\mathcal{P}2/16$	2.14E-02	-	3.38E-05	-	5.96E-04	-	2.61	1.12	9.01E-03	-	20.6	1.19
$\mathcal{P}2/32$	2.92E-03	2.86	2.57E-06	3.72	2.65E-05	4.49	0.70	1.10	1.18E-03	2.94	11.8	1.13
$\mathcal{P}2/64$	3.77E-04	2.95	2.27E-07	3.51	1.09E-06	4.59	0.16	1.08	1.40E-04	3.07	6.48	1.11
$\mathcal{P}2/128$	4.72E-05	2.99	2.83E-08	3.00	1.61E-07	2.77	0.03	1.03	1.55E-05	3.17	3.41	1.07
$\mathcal{P}3/16$	1.39E-03	-	2.26E-06	-	3.50E-04	-	2.66	1.03	1.21E-03	-	74.9	1.29
$\mathcal{P}3/32$	9.60E-05	3.85	8.92E-08	4.67	1.53E-05	4.51	0.70	1.02	6.17E-05	4.30	44.6	1.15
$\mathcal{P}3/64$	6.71E-06	3.84	5.71E-09	3.96	5.44E-07	4.81	0.16	1.03	3.21E-06	4.26	24.0	1.11
$\mathcal{P}3/128$	5.15E-07	3.70	2.92E-10	4.29	1.78E-08	4.93	0.02	1.01	2.73E-07	3.56	12.4	1.09
$\mathcal{P}4/8$	2.85E-02	-	9.78E-07	-	2.49E-03	-	10.6	-	3.84E-02	-	100	1.46
$\mathcal{P}4/16$	1.27E-03	4.49	2.20E-08	5.47	2.86E-05	6.45	2.66	1.04	1.67E-03	4.52	100	1.58
$\mathcal{P}4/32$	4.59E-05	4.79	4.20E-10	5.71	2.79E-07	6.68	0.70	1.03	6.62E-05	4.66	87.8	1.39
$\mathcal{P}4/64$	1.64E-06	4.81	1.74E-11	4.60	2.36E-09	6.89	0.17	1.02	2.97E-06	4.48	65.0	1.26
Hybrid Mesh	e_{L^2}	$\mathcal{O}_{L^2}$	e_{L^2}	$\mathcal{O}_{L^2}$	e_{L^2}	$\mathcal{O}_{L^2}$	% troub. cells	CPU	e_{L^2}	$\mathcal{O}_{L^2}$	% troub. cells	CPU
$\mathcal{P}2/16$	4.52E-02	-	1.58E-04	-	4.18E-03	-	3.31	1.13	1.56E-02	-	22.7	1.20
$\mathcal{P}2/32$	6.08E-03	2.88	2.25E-05	2.81	8.69E-04	2.27	0.87	1.10	1.90E-03	3.04	12.6	1.13
$\mathcal{P}2/64$	7.61E-04	3.01	2.67E-06	3.07	5.03E-05	4.11	0.22	1.02	2.29E-04	3.05	7.06	1.04
$\mathcal{P}2/128$	9.55E-05	2.99	4.30E-07	2.63	1.75E-06	4.85	0.06	1.01	2.64E-05	3.12	3.74	1.03
$\mathcal{P}3/16$	3.49E-03	-	4.22E-06	-	5.15E-04	-	3.42	1.04	3.55E-03	-	85.4	1.27
$\mathcal{P}3/32$	1.62E-04	4.43	4.36E-07	3.28	5.22E-05	3.30	0.85	1.03	1.63E-04	4.45	52.3	1.16
$\mathcal{P}3/64$	1.04E-05	3.96	2.97E-08	3.87	5.06E-07	6.69	0.20	1.07	8.89E-06	4.20	28.4	1.15
$\mathcal{P}3/128$	7.50E-07	3.80	2.04E-09	3.86	3.21E-08	3.98	0.04	1.00	5.90E-07	3.91	14.7	1.05
$\mathcal{P}4/8$	6.39E-02	-	5.13E-06	-	6.66E-03	-	13.9	1.03	9.01E-02	-	100	1.47
$\mathcal{P}4/16$	3.13E-03	4.35	1.61E-07	4.99	1.04E-04	6.00	3.47	1.04	4.76E-03	4.24	100	1.56
$\mathcal{P}4/32$	1.07E-04	4.88	6.06E-09	4.73	1.16E-06	6.49	0.86	1.02	1.69E-04	4.82	91.9	1.36
$\mathcal{P}4/64$	3.37E-06	4.98	2.80E-10	4.44	2.53E-08	5.52	0.20	1.02	6.81E-06	4.63	70.6	1.28

Table B.4
Values for e_{L^∞} and e_{L^2} error and convergence rates for smooth profile advection test with hybrid DG-FV scheme when all the cells are artificially rendered as troubled.

DG/CWENOZ all cells troubled	$\mathcal{P}2$				$\mathcal{P}3$				$\mathcal{P}4$			
Number of Edges	e_{L^∞}	$\mathcal{O}_{L^\infty}$	e_{L^2}	$\mathcal{O}_{L^2}$	e_{L^∞}	$\mathcal{O}_{L^\infty}$	e_{L^2}	$\mathcal{O}_{L^2}$	e_{L^∞}	$\mathcal{O}_{L^\infty}$	e_{L^2}	$\mathcal{O}_{L^2}$
16	2.12E-01	-	1.07E-01	-	1.61E-02	-	8.40E-03	-	3.00E-02	-	1.51E-02	-
32	3.12E-02	2.77	1.56E-02	2.78	7.85E-04	4.36	4.28E-04	4.30	1.04E-03	4.85	5.21E-04	4.86
64	4.02E-03	2.96	2.02E-03	2.95	4.21E-05	4.22	2.48E-05	4.11	3.34E-05	4.97	1.66E-05	4.97
128	5.02E-04	3.00	2.51E-04	3.01	2.48E-06	4.08	1.51E-06	4.04	1.05E-06	4.99	5.25E-07	4.99

referred as CPU, which is normalized by the time taken by the pure DG scheme with the same polynomial order and mesh resolution.

We noted that on unstructured meshes, the increase in computational time is negligible as long as the percentage of troubled cells is contained within the 20%.

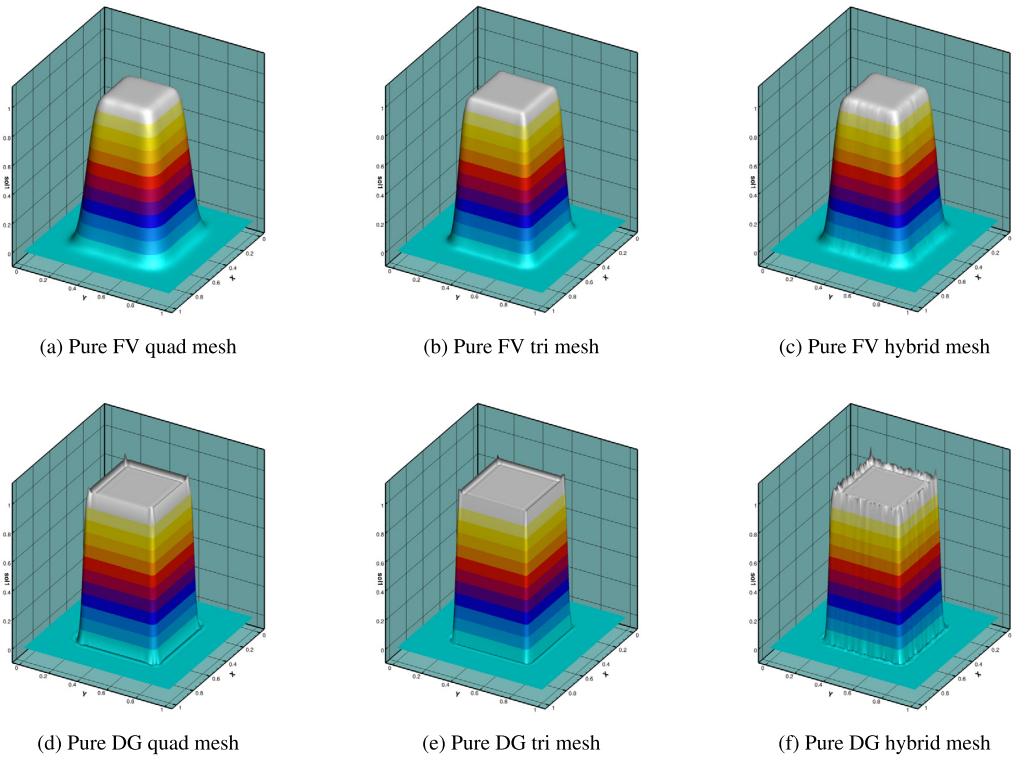

(a) Pure FV quad mesh (b) Pure FV tri mesh (c) Pure FV hybrid mesh

(d) Pure DG quad mesh (e) Pure DG tri mesh (f) Pure DG hybrid mesh

Fig. C.25. Computed results for the advection of step profile on different meshes with. The performance of the pure 3^{rd} order FV and DG schemes are compared with the hybrid 3^{rd} order DG/FV (DG($\mathcal{P}2$)-FV(CWENOZ3)) schemes using different troubled cell indicators.

Appendix C. Advection of discontinuous profile

The non-oscillatory performance of the hybrid scheme is now assessed against the advection of a discontinuous profile. A square profile in two dimensions is advected for one period $t = 1$ and is defined by the following initial conditions:

$$\mathbf{f}(x, y) = \begin{cases} 1, & \text{if } (x, y) \in [0.2, 0.8], \\ 0, & \text{if otherwise.} \end{cases} \tag{C.1}$$

The computational domain is again given by $[0, 10] \times [0, 10]$ with periodic boundary conditions applied on all sides, and the computations are performed on the uniform and unstructured meshes with a resolution corresponding to 64 edges per side. The results obtained with the pure FV, DG, and with the hybrid DG-FV scheme with the MOOD type indicators with two different threshold values, for a 3rd order scheme, are presented in Fig. C.25. It can be observed that the pure DG better preserves the initial profile after one period, compared to the pure FV which has a more diffused profile.

On the other hand the pure DG scheme produces overshoots at the base and at the edges of the profile, especially on the hybrid mesh. In order to dampen the oscillations, the hybrid scheme is tested with two threshold values, i.e. taking a value for $\alpha = 10^{-3}$ from the MOOD implementation of [27] and the relaxed value $\alpha = 10^{-1}$ of the implementation of [28], and the indicators will be referred as MOOD^O and MOOD^R respectively. In addition, the two bounds definitions discussed in Appendix A will be used with said indicators, and therefore MOOD^O_X and MOOD^R_X will refer to the extended bound setting, while MOOD^O_L and MOOD^R_L refer to the version with bounds limited to target cell's direct side neighbours.

The time history of the total percentage of troubled cells is plotted in Fig. C.26. The configuration with bounds limited to the neighbouring cells results in a higher number of cells marked as troubled, regardless of the selected threshold value. As expected, extending the bounds to the entire stencil or setting a smaller value for the threshold value, such as for the MOOD^R_X, results in fewer invalid cells detected, which is beneficial for the final accuracy but is not sufficient to avoid some oscillations at the edges of the profile. On the other hand, the MOOD^O_X seems to be in this case the best compromise to preserve the original accuracy provided by the DG scheme, without producing any oscillation. Importantly, we note the similarity of the final results provided by the MOOD^O_X and MOOD^R_L, thus allowing the choice between a more conservative threshold value and the extended bound setting, or a more permissive value with a limited bound range.

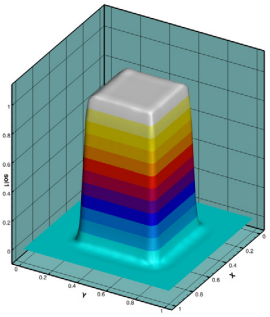

(g) MOOD_X^O quad mesh

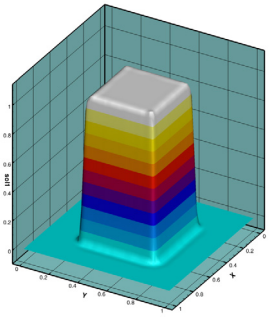

(h) MOOD_X^O tri mesh

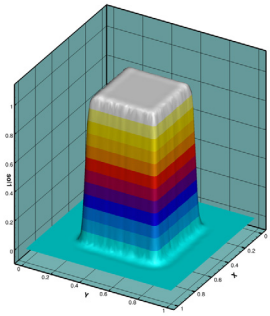

(i) MOOD_X^O hybrid mesh

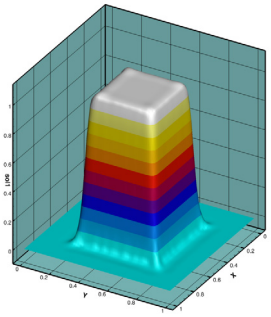

(j) MOOD_L^O quad mesh

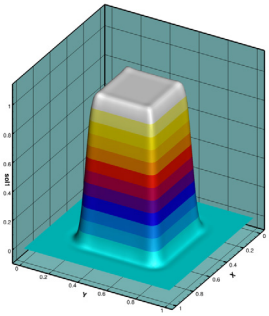

(k) MOOD_L^O tri mesh

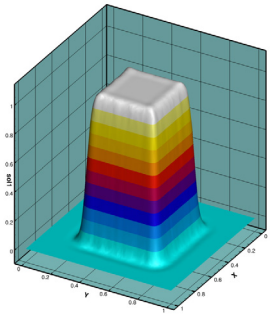

(l) MOOD_L^O hybrid mesh

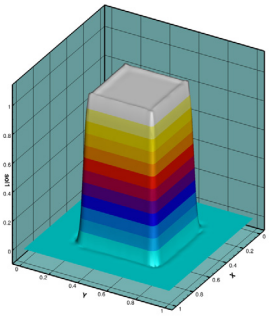

(m) MOOD_X^R quad mesh

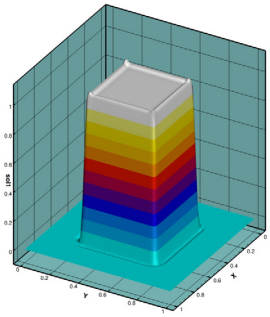

(n) MOOD_X^R tri mesh

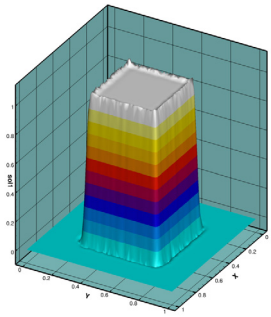

(o) MOOD_X^R hybrid mesh

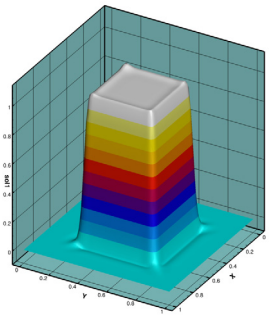

(p) MOOD_L^R quad mesh

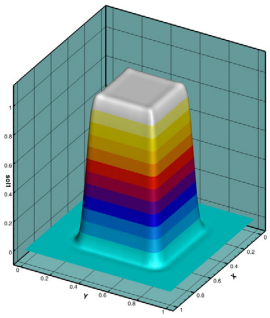

(q) MOOD_L^R tri mesh

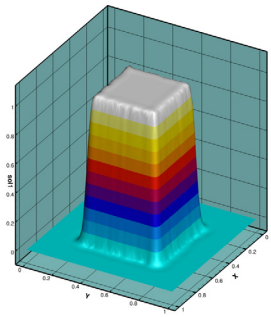

(r) MOOD_L^R hybrid mesh

Fig. C.25. (*continued*)

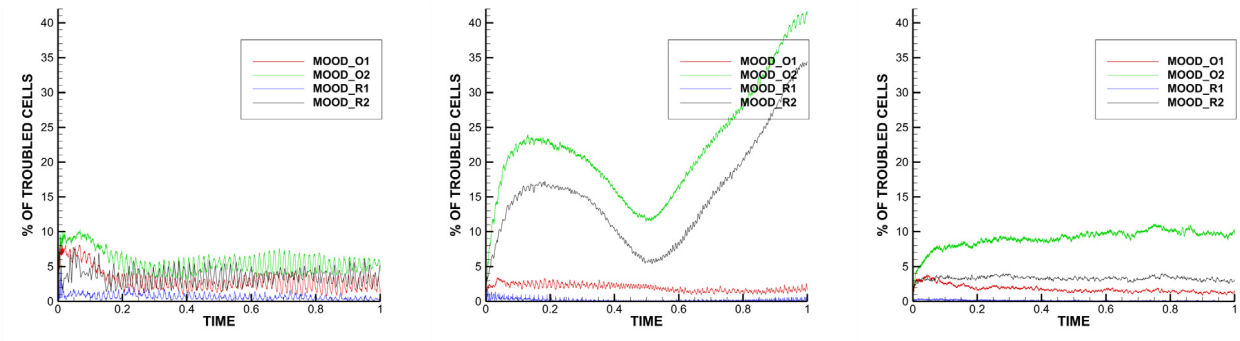

(a) Quadrilateral mesh (b) Triangular mesh (c) Hybrid mesh

Fig. C.26. Troubled cell trends on different meshes comparing different troubled cell indicators.

References

[1] W.H. Reed, T.R. Hill, Triangular Mesh Methods for the Neutron Transport Equation, Tech. Rep., Los Alamos Scientific Laboratory, 1973.
[2] B. Cockburn, C.-W. Shu, Runge-Kutta discontinuous Galerkin methods for convection-dominated problems, J. Sci. Comput. 16 (3) (2001) 173–261.
[3] B. Cockburn, C.-W. Shu, TVB Runge-Kutta projection discontinous Galerkin finite element methods II, 1989.
[4] B. Cockburn, S.Y. Lin, C.W. Shu, TVB Runge-Kutta local projection discontinuous Galerkin finite element method for conservation laws III: one-dimensional systems, J. Comput. Phys. 84 (1) (1989) 90–113, https://doi.org/10.1016/0021-9991(89)90183-6.
[5] G. Jiang, C.-W. Shu, On a cell entropy inequality for discontinuous Galerkin methods, Math. Comput. 62 (206) (1994) 531, https://doi.org/10.2307/2153521.
[6] B. Cockburn, C.W. Shu, The Runge-Kutta discontinuous Galerkin method for conservation laws V, J. Comput. Phys. 141 (2) (1998) 199–224.
[7] R. Biswas, K.D. Devine Parallel, Adaptive finite element methods for conservation laws, Appl. Numer. Math. 9274 (93) (1994).
[8] A. Burbeau, P. Sagaut, C.H. Bruneau, A problem-independent limiter for high-order Runge-Kutta discontinuous Galerkin methods, J. Comput. Phys. 169 (1) (2001) 111–150, https://doi.org/10.1006/jcph.2001.6718.
[9] V. Titarev, E. Toro, Finite-volume WENO schemes for three-dimensional conservation laws, J. Comput. Phys. 201 (1) (2004) 238–260.
[10] C.-W. Shu, S. Osher, Efficient implementation of essentially non-oscillatory shock-capturing schemes, II, J. Comput. Phys. 83 (1) (1989) 32–78.
[11] A. Harten, B. Enquist, S. Osher, S.R. Chakravarthy, Uniformly high order accurate essentially non-oscillatory schemes, III, J. Comput. Phys. 71 (2) (1987) 231–303.
[12] G.S. Jiang, C.W. Shu, Efficient implementation of weighted ENO schemes, J. Comput. Phys. 126 (1) (1996) 202–228.
[13] J. Fernandez-Fidalgo, L. Ramirez, P. Tsoutsanis, I. Colominas, X. Nogueira, A reduced-dissipation WENO scheme with automatic dissipation adjustment, J. Comput. Phys. 425 (2021), https://doi.org/10.1016/j.jcp.2020.109749.
[14] D. Levy, G. Puppo, G. Russo, O.F.C. Laws, Central WENO Schemes for Hyperbolic Systems of Conservation Laws, Mathematical Modelling and Numerical Analysis, 1999.
[15] D. Levy, G. Puppo, G. Russo, Compact central WENO schemes for multidimensional conservation laws, SIAM J. Sci. Comput. 22 (2000) 656–672.
[16] D. Levy, S. Nayak, C.-W. Shu, Y.-T. Zhang, Central WENO schemes for Hamilton-Jacobi equations on triangular meshes, SIAM J. Sci. Comput. 28 (6) (2006) 2229–2247.
[17] R. Borges, M. Carmona, B. Costa, W. Don, An improved weighted essentially non-oscillatory scheme for hyperbolic conservation laws, J. Comput. Phys. 227 (2008) 3191–3211.
[18] M. Castro, B. Costa, W. Don, High order weighted essentially non-oscillatory WENO-Z schemes for hyperbolic conservation laws, J. Comput. Phys. 230 (2011) 1766–1792.
[19] J. Qiu, C.-W. Shu, Runge-Kutta discontinuous Galerkin method using WENO limiters, SIAM J. Sci. Comput. 26 (2005) 907–929, https://doi.org/10.1137/S1064827503425298.
[20] J. Zhu, C.-W. Shu, J. Qiu, High-order Runge-Kutta discontinuous Galerkin methods with a new type of multi-resolution WENO limiters on triangular meshes, Appl. Numer. Math. 153 (2020) 519–539, https://doi.org/10.1016/j.apnum.2020.03.013.
[21] H. Zhu, J. Qiu, J. Zhu, A simple, high-order and compact WENO limiter for RKDG method, Comput. Math. Appl. 79 (2) (2020) 317–336, https://doi.org/10.1016/j.camwa.2019.06.034.
[22] J. Zhu, J. Qiu, Hermite WENO schemes and their application as limiters for Runge-Kutta discontinuous Galerkin method, III: unstructured meshes, J. Sci. Comput. 39 (2) (2009) 293–321.
[23] L. Krivodonova, J. Xin, J.F. Remacle, N. Chevaugeon, J.E. Flaherty, Shock detection and limiting with discontinuous Galerkin methods for hyperbolic conservation laws, Appl. Numer. Math. 48 (3–4) (2004) 323–338, https://doi.org/10.1016/j.apnum.2003.11.002.
[24] G. Fu, C.W. Shu, A new troubled-cell indicator for discontinuous Galerkin methods for hyperbolic conservation laws, J. Comput. Phys. 347 (2017) 305–327, https://doi.org/10.1016/j.jcp.2017.06.046.
[25] S. Diot, R. Loubère, S. Clain, The multidimensional optimal order detection method in the three-dimensional case: very high-order finite volume method for hyperbolic systems, Int. J. Numer. Methods Fluids 73 (4) (2013) 362–392, https://doi.org/10.1002/fld.3804.
[26] S. Clain, S. Diot, R. Loubére, A high-order finite volume method for systems of conservation laws-multi-dimensional optimal order detection (MOOD), J. Comput. Phys. 230 (10) (2011) 4028–4050, https://doi.org/10.1016/j.jcp.2011.02.026.
[27] S. Diot, S. Clain, R. Loubére, Improved detection criteria for the multi-dimensional optimal order detection (MOOD) on unstructured meshes with very high-order polynomials, Comput. Fluids 64 (2012) 43–63, https://doi.org/10.1016/j.compfluid.2012.05.004.
[28] P. Farmakis, P. Tsoutsanis, X. Nogueira, WENO schemes on unstructured meshes using a relaxed a posteriori MOOD limiting approach, Comput. Methods Appl. Mech. Eng. 363 (2020), https://doi.org/10.1016/j.cma.2020.112921.
[29] P. Tsoutsanis, M.S.S. Pavan Kumar, P.S. Farmakis, A relaxed a posteriori mood algorithm for multicomponent compressible flows using high-order finite-volume methods on unstructured meshes, Appl. Math. Comput. 437 (2023) 127544, https://doi.org/10.1016/j.amc.2022.127544.
[30] P. Tsoutsanis, Extended bounds limiter for high-order finite-volume schemes on unstructured meshes, J. Comput. Phys. 362 (2018) 69–94.
[31] UCNS3D CFD code, http://www.ucns3d.com. (Accessed 5 May 2022).
[32] A.F. Antoniadis, D. Drikakis, P.S. Farmakis, L. Fu, I. Kokkinakis, X. Nogueira, P.A. Silva, M. Skote, V. Titarev, P. Tsoutsanis, UCNS3D: an open-source high-order finite-volume unstructured cfd solver, Comput. Phys. Commun. 279 (2022) 108453, https://doi.org/10.1016/j.cpc.2022.108453.

[33] H. Luo, J.D. Baum, R. Löhner, A discontinuous Galerkin method based on a Taylor basis for the compressible flows on arbitrary grids, J. Comput. Phys. 227 (20) (2008) 8875–8893, https://doi.org/10.1016/j.jcp.2008.06.035.
[34] H. Luo, L. Luo, R. Nourgaliev, V.A. Mousseau, N. Dinh, A reconstructed discontinuous Galerkin method for the compressible Navier-Stokes equations on arbitrary grids, J. Comput. Phys. 229 (19) (2010) 6961–6978, https://doi.org/10.1016/j.jcp.2010.05.033.
[35] W. Boscheri, G. Dimarco, High order modal discontinuous Galerkin implicit-explicit Runge Kutta and linear multistep schemes for the Boltzmann model on general polygonal meshes, Comput. Fluids 233 (2022) 105224.
[36] E. Gaburro, W. Boscheri, S. Chiocchetti, C. Klingenberg, V. Springel, M. Dumbser, High order direct arbitrary-Lagrangian-Eulerian schemes on moving Voronoi meshes with topology changes, J. Comput. Phys. 407 (2020) 109167.
[37] P. Tsoutsanis, V. Titarev, D. Drikakis, WENO schemes on arbitrary mixed-element unstructured meshes in three space dimensions, J. Comput. Phys. 230 (4) (2011) 1585–1601.
[38] V. Titarev, P. Tsoutsanis, D. Drikakis, WENO schemes for mixed-element unstructured meshes, Commun. Comput. Phys. 8 (3) (2010) 585–609.
[39] M. Dumbser, M. Kaser, V. Titarev, E. Toro, Quadrature-free non-oscillatory finite volume schemes on unstructured meshes for nonlinear hyperbolic systems, J. Comput. Phys. 226 (1) (2007) 204–243.
[40] P. Tsoutsanis, M. Dumbser, Arbitrary high order central non-oscillatory schemes on mixed-element unstructured meshes, Comput. Fluids 225 (2021), https://doi.org/10.1016/j.compfluid.2021.104961.
[41] P. Tsoutsanis, A. Antoniadis, D. Drikakis, WENO schemes on arbitrary unstructured meshes for laminar, transitional and turbulent flows, J. Comput. Phys. 256 (2014) 254–276.
[42] P. Tsoutsanis, D. Drikakis, A high-order finite-volume method for atmospheric flows on unstructured grids, J. Coupled Syst. Multiscale Dyn. 4 (2016) 170–186, https://doi.org/10.1166/jcsmd.2016.1104.
[43] A. Antoniadis, P. Tsoutsanis, D. Drikakis, Numerical accuracy in RANS computations of high-lift multi-element airfoil and aircraft configurations, in: 53rd AIAA Aerospace Sciences Meeting, vol. 0317, 2015.
[44] A. Antoniadis, P. Tsoutsanis, D. Drikakis, High-order schemes on mixed-element unstructured grids for aerodynamic flows, in: 42nd AIAA Fluid Dynamics Conference and Exhibit, vol. 2833, 2012.
[45] A. Antoniadis, P. Tsoutsanis, I. Kokkinakis, Z. Rana, D. Drikakis Azure, An advanced CFD software suite based on high-resolution and high-order methods, in: 53rd AIAA Aerospace Sciences Meeting, vol. 0813, 2015.
[46] A. Antoniadis, D. Drikakis, I.W. Kokkinakis, P. Tsoutsanis, Z. Rana, High-order methods for hypersonic shock wave turbulent boundary layer interaction flow, in: 20th AIAA International Space Planes and Hypersonic Systems and Technologies Conference, vol. 3524, 2015.
[47] P. Tsoutsanis, I. Kokkinakis, L. Konozsy, D. Drikakis, R. Williams, D. Youngs, Comparison of structured- and unstructured-grid, compressible and incompressible methods using the vortex pairing problem, Comput. Methods Appl. Mech. Eng. 293 (2015) 207–231, https://doi.org/10.1016/j.cma.2015.04.010.
[48] P. Tsoutsanis, H. Srinivasan, Adaptive mesh refinement techniques for high-order finite-volume WENO schemes, in: ECCOMAS Congress 2016, Crete, Greece, 2016.
[49] P. Tsoutsanis, N. Simmonds, A. Gaylard, Implementation of a low-Mach number modification for high-order finite-volume schemes for arbitrary hybrid unstructured meshes, in: ECCOMAS Congress 2016, Crete, Greece, 2016.
[50] P. Tsoutsanis, D. Drikakis, Addressing the challenges of implementation of high-order finite-volume schemes for atmospheric dynamics on unstructured meshes, in: ECCOMAS Congress 2016, Crete, Greece, 2016.
[51] P. Tsoutsanis, A. Antoniadis, K. Jenkins, Improvement of the computational performance of a parallel unstructured WENO finite volume CFD code for implicit large Eddy simulation, Comput. Fluids 173 (2018) 157–170, https://doi.org/10.1016/j.compfluid.2018.03.012.
[52] N. Simmonds, P. Tsoutsanis, A. Antoniadis, K. Jenkins, A. Gaylard, Low-Mach number treatment for finite-volume schemes on unstructured meshes, Appl. Math. Comput. 336 (2018) 368–393.
[53] F. Ricci, P. Silva, P. Tsoutsanis, A. Antoniadis, Hovering rotor solutions by high-order methods on unstructured grids, Aerosp. Sci. Technol. 97 (2020), https://doi.org/10.1016/j.ast.2019.105648.
[54] P. Silva, P. Tsoutsanis, A. Antoniadis, Simple multiple reference frame for high-order solution of hovering rotors with and without ground effect, Aerosp. Sci. Technol. 111 (2021), https://doi.org/10.1016/j.ast.2021.106518.
[55] P. Tsoutsanis, Stencil selection algorithms for WENO schemes on unstructured meshes, J. Comput. Phys.: X 4 (2019), https://doi.org/10.1016/j.jcpx.2019.100037.
[56] P. Tsoutsanis, E.M. Adebayo, A. Carriba Merino, A. Perez Arjona, M. Skote, CWENO finite-volume interface capturing schemes for multicomponent flows using unstructured meshes, J. Sci. Comput. 89 (2021), https://doi.org/10.1007/s10915-021-01673-y.
[57] A.F. Antoniadis, P. Tsoutsanis, D. Drikakis, Assessment of high-order finite volume methods on unstructured meshes for rans solutions of aeronautical configurations, Comput. Fluids 146 (2017) 86–104, https://doi.org/10.1016/j.compfluid.2017.01.002.
[58] P. Silva, P. Tsoutsanis, A. Antoniadis, Numerical investigation of full helicopter with and without the ground effect, Aerosp. Sci. Technol. 122 (2022), https://doi.org/10.1016/j.ast.2022.107401.
[59] A. Jalali, C. Ollivier-Gooch, Higher-order finite volume solution reconstruction on highly anisotropic meshes, in: 21st AIAA Computational Fluid Dynamics Conference, 2013.
[60] M. Dumbser, M. Castro, C. Pares, E. Toro, ADER schemes on unstructured meshes for nonconservative hyperbolic systems: applications to geophysical flows, Comput. Fluids 38 (9) (2009) 1731–1748.
[61] X. Nogueira, L. Cueto-Felgueroso, I. Colominas, F. Navarrina, M. Casteleiro, A new shock-capturing technique based on moving least squares for higher-order numerical schemes on unstructured grids, Comput. Methods Appl. Mech. Eng. 199 (37–40) (2010) 2544–2558.
[62] G.W. Stewart, Matrix Algorithms, Volume 1: Basic Decompositions, Society for Industrial and Applied Mathematics SIAM, 1998.
[63] E. Toro, M. Spruce, W. Speares, Restoration of the contact surface in the HLL-Riemann solver, Shock Waves 4 (1) (1994) 25–34.
[64] A. Stroud, Approximate Calculation of Multiple Integrals, Prentice-Hall Inc., Englewood Cliffs, New Jersey, 1971.
[65] P. Tsoutsanis, Knl performance comparison UCNS3D, ARCHER performance report, 2017, 157–170, www.archer.ac.uk/community/benchmarks/archer-knl/KNLperfUCNS3D.pdf.
[66] M. Dumbser, O. Zanotti, R. Loubère, S. Diot, A posteriori subcell limiting of the discontinuous Galerkin finite element method for hyperbolic conservation laws, J. Comput. Phys. 278 (2014) 47–75, https://doi.org/10.1016/j.jcp.2014.08.009, arXiv:1406.7416.
[67] F. Vilar, A posteriori correction of high-order discontinuous Galerkin scheme through subcell finite volume formulation and flux reconstruction, J. Comput. Phys. 387 (2019) 245–279, https://doi.org/10.1016/j.jcp.2018.10.050.
[68] A. Huerta, E. Casoni, J. Peraire, A simple shock-capturing technique for high-order discontinuous Galerkin methods, Int. J. Numer. Methods Fluids 69 (10) (2012) 1614–1632, https://doi.org/10.1002/fld.2654.
[69] S. Busto, S. Chiocchetti, M. Dumbser, E. Gaburro, I. Peshkov, High order ADER schemes for continuum mechanics, Front. Phys. 8 (2020) 32, https://doi.org/10.3389/fphy.2020.00032.
[70] J. Qiu, C. Shu, A comparison of troubled cell indicators for Runge-Kutta discontinuous Galerkin methods using WENO limiters, SIAM J. Sci. Comput. 27 (2005) 995–1013.
[71] J. Fernández-Fidalgo, X. Nogueira, L. Ramírez, I. Colominas, An a posteriori, efficient, high-spectral resolution hybrid finite-difference method for compressible flows, Comput. Methods Appl. Mech. Eng. 335 (2018) 91–127, https://doi.org/10.1016/j.cma.2018.02.013.

[72] D. Balsara, C.-W. Shu, Monotonicity preserving weighted essentially non-oscillatory schemes with increasingly high order of accuracy, J. Comput. Phys. 160 (2) (2000) 405–452.
[73] R. Leveque, High-resolution conservative algorithms for advection in incompressible flow, SIAM J. Numer. Anal. 33 (2) (1996) 627–665, https://doi.org/10.1137/0733033.
[74] P. Woodward, P. Colella, The numerical simulation of two-dimensional fluid flow with strong shocks, J. Comput. Phys. 54 (1) (1984) 115–173.
[75] H. Li, G. Ben-Dor, Analysis of double-Mach-reflection wave configurations with convexly curved Mach stems, Shock Waves 9 (1999) 319–326.
[76] A.N. Semenov, M.K. Berezkina, I.V. Krassovskaya, Classification of pseudo-steady shock wave reflection types, Shock Waves 22 (2012) 307–316.
[77] H. Schardin, High frequency cinematography in the shock tube, J. Photogr. Sci. 2 (1957) 17–19.
[78] S.-M. Chang, K.-S. Chang, On the shock vortex-interaction in Schardin's problem, Shock Waves 10 (2000) 333–343.
[79] D. Drikakis, C. Fureby, F. Grinstein, D. Youngs, Simulation of transition and turbulence decay in the Taylor-Green vortex, J. Turbul. 8 (2007) 1–12.
[80] J. Bull, A. Jameson, Simulation of the Taylor-Green vortex using high-order flux reconstruction schemes, AIAA J. 53 (9) (2015) 2750–2761.
[81] M. Dumbser, I. Peshkov, E. Romenski, O. Zanotti, High order ADER schemes for a unified first order hyperbolic formulation of continuum mechanics: viscous heat-conducting fluids and elastic solids, J. Comput. Phys. 314 (2016) 824–862.
[82] J.-B. Chapelier, M. de la Llave Plata, E. Lamballais, Development of a multiscale LES model in the context of a modal discontinuous Galerkin method, Comput. Methods Appl. Mech. Eng. 307 (2016) 275–299.
[83] A. Sifounakis, S. Lee, D. You, A conservative finite volume method for incompressible Navier-Stokes equations on locally refined nested Cartesian grids, J. Comput. Phys. 326 (2016) 845–861.
[84] C.-W. Shu, W.-S. Don, D. Gottlieb, O. Schilling, L. Jameson, Numerical convergence study of nearly incompressible, inviscid Taylor-Green vortex flow, J. Sci. Comput. 24 (1) (2005) 569–595.
[85] B. Vermeire, F. Witherden, P. Vincent, On the utility of GPU accelerated high-order methods for unsteady flow simulations: a comparison with industry-standard tools, J. Comput. Phys. 334 (2017) 497–521.
[86] F. Fambri, M. Dumbser, Spectral semi-implicit and space-time discontinuous Galerkin methods for the incompressible Navier-Stokes equations on staggered Cartesian grids, Appl. Numer. Math. 110 (2016) 41–74.
[87] F. Fambri, M. Dumbser, Semi-implicit discontinuous Galerkin methods for the incompressible Navier-Stokes equations on adaptive staggered Cartesian grids, Comput. Methods Appl. Mech. Eng. 324 (2017) 170–203.
[88] M. Tavelli, M. Dumbser, A staggered space-time discontinuous Galerkin method for the three-dimensional incompressible Navier-Stokes equations on unstructured tetrahedral meshes, J. Comput. Phys. 319 (2016) 294–323.
[89] M. Tavelli, M. Dumbser, A pressure-based semi-implicit space-time discontinuous Galerkin method on staggered unstructured meshes for the solution of the compressible Navier-Stokes equations at all Mach numbers, J. Comput. Phys. 341 (2017) 341–376.
[90] M. Brachet, D. Meiron, B. Nickel, R. Morf, U. Frisch, S. Orszag, Small-scale structure of the Taylor-Green vortex, J. Fluid Mech. 130 (1983) 411–452, https://doi.org/10.1017/S0022112083001159.
[91] A. Winters, R. Moura, G. Mengaldo, G. Gassner, S. Walch, J. Peiro, S. Sherwin, A comparative study on polynomial dealiasing and split form discontinuous Galerkin schemes for under-resolved turbulence computations, J. Comput. Phys. 372 (2018) 1–21, https://doi.org/10.1016/j.jcp.2018.06.016.
[92] R. Moura, G. Mengaldo, J. Peiro, S. Sherwin, On the Eddy-resolving capability of high-order discontinuous Galerkin approaches to implicit les / under-resolved dns of Euler turbulence, J. Comput. Phys. 330 (2017) 615–623, https://doi.org/10.1016/j.jcp.2016.10.056.
[93] J.-B. Chapelier, M. De La Llave Plata, F. Renac, Inviscid and viscous simulations of the Taylor-Green vortex flow using a modal discontinuous Galerkin approach, https://doi.org/10.2514/6.2012-3073, 2012.
[94] G. Gassner, D. Kopriva, A comparison of the dispersion and dissipation errors of Gauss and Gauss-Lobatto discontinuous Galerkin spectral element methods, SIAM J. Sci. Comput. 33 (5) (2011) 2560–2579, https://doi.org/10.1137/100807211.
[95] D. Flad, A. Beck, C.-D. Munz, Simulation of underresolved turbulent flows by adaptive filtering using the high order discontinuous Galerkin spectral element method, J. Comput. Phys. 313 (2016) 1–12, https://doi.org/10.1016/j.jcp.2015.11.064.
[96] G. Gassner, A. Winters, A novel robust strategy for discontinuous Galerkin methods in computational fluid mechanics: why? when? what? where?, Front. Phys. 8 (2021), https://doi.org/10.3389/fphy.2020.500690.
[97] D. Lusher, N. Sandham, Assessment of low-dissipative shock-capturing schemes for the compressible Taylor-Green vortex, AIAA J. 59 (2) (2021) 533–545, https://doi.org/10.2514/1.J059672.
[98] M. Park, J. Morgenstern, Summary and statistical analysis of the first AIAA sonic boom prediction workshop, J. Aircr. 53 (2) (2016) 578–598, https://doi.org/10.2514/1.C033449.
[99] K. Michalak, C. Ollivier-Gooch, Limiters for unstructured higher-order accurate solutions of the Euler equations, in: 46th AIAA Aerospace Sciences Meeting and Exhibit, 2008.

2022-11-11

Hybrid discontinuous Galerkin-finite volume techniques for compressible flows on unstructured meshes

Maltsev, Vadim

Elsevier

Maltsev V, Yuan D, Jenkins KW, et al., (2023) Hybrid discontinuous Galerkin-finite volume techniques for compressible flows on unstructured meshes. Journal of Computational Physics, Volume 473, January 2023, Article number 111755

https://doi.org/10.1016/j.jcp.2022.111755